Hindawi
International Journal of Energy Research
Volume 2024, Article ID 8316781, 22 pages
https://doi.org/10.1155/2024/8316781

*Research Article*

# Performance Prediction and Optimization of Single-Piston Free Piston Expander-Linear Generator Based on Machine Learning and Genetic Algorithm

**Jian Li,[1] Zhengxing Zuo,[1] Boru Jia,[1] Huihua Feng,[1] Hongguang Zhang,[2] and Bingang Mei[1]**

[1]*School of Mechanical Engineering, Beijing Institute of Technology, Beijing 100081, China*
[2]*Key Laboratory of Enhanced Heat Transfer and Energy Conservation of MOE, Beijing Key Laboratory of Heat Transfer and Energy Conversion, Faculty of Environment and Life, Beijing University of Technology, Beijing 100124, China*

Correspondence should be addressed to Boru Jia; boru.jia@bit.edu.cn and Huihua Feng; fenghh@bit.edu.cn

Received 22 July 2023; Revised 14 February 2024; Accepted 23 February 2024; Published 8 March 2024

Academic Editor: Mohamed Louzazni



This paper proposed a single-piston free piston expander-linear generator (SFPE-LG) prototype applied to organic Rankine cycle systems. Two valve timing control strategies, namely, time control strategy (TCS) and position control strategy (PCS), were developed. Based on the experimental data, a back propagation neural network (BPNN) prediction model was established. The effects of structural parameters such as neural network layers, transfer function, training function, hidden layer nodes, and learning rate on the prediction accuracy of this BPNN model were discussed. The training and prediction accuracy of the BPNN model was verified using 5-fold cross-validation and Wilcoxon signed-rank test. Moreover, the BPNN model was integrated with a genetic algorithm to predict and optimize the maximum output power of the SFPE-LG. The results showed that the BPNN model used to predict the motion characteristics and output performance of the SFPE-LG exhibits strong learning ability and high prediction accuracy. Notably, the prediction accuracy of the BPNN model is significantly higher under the PCS compared to TCS. The effect of hidden layer nodes on mean square error (MSE) and correlation coefficient ($R$) is greater than that of the learning rate. When the number of hidden layer nodes exceeds 30, the BPNN model consistently achieves low MSE and high $R$. The optimization results showed that the SFPE-LG can obtain a maximum output power of 141.69 W under the TCS, when the working parameters are inlet pressure of 0.7 MPa, intake duration of 35 ms, load resistance of 67 Ω, and expansion duration of 104 ms, respectively.

## 1. Introduction

Nowadays, various new energy vehicles have been vigorously developed in many countries around the world. However, it is still essential to carry out pollution prevention, energy saving, and emission reduction for internal combustion engine (ICE) vehicles, which account for a large proportion of vehicles. Generally, the heat generated by the combustion in an ICE cannot be fully converted into useful power to be output. Only 20%~45% of the heat generated by combustion is used for power output, and most of the remaining energy is dissipated as heat energy [1, 2]. Among them, the energy dissipated by the exhaust system accounts for about 40%~45% (gasoline engines) and 35%~40% (diesel engines) of the total energy. Meanwhile, the exhaust temperature of an ICE can reach 700~1100 K [3–5]. Thus, the recovery and utilization for this waste heat energy from automotive ICEs are effective methods to reduce fuel consumption and improve energy conversion efficiency. At present, the waste heat utilization technologies of ICEs mainly include thermoelectric power generation, air Brayton cycle, turbocharging, waste heat refrigeration, and organic Rankine cycle (ORC) [6, 7].

In the medium- and low-temperature waste heat recovery, ORC systems have been widely adopted in multiple fields due to their structural simplicity, easy maintenance, and good reliability [8, 9]. Research on recovering waste heat

from automotive ICEs using Rankine cycle began in the 1970s, when water was adopted as the working medium. Since then, the ORC waste heat recovery systems for automotive ICEs have been continuously improved and developed. Many research papers and patents have been published on ORC waste heat recovery in automobile ICEs, but there are no actual and large-scale commercial applications of ORC systems in automobiles [10–12]. One of the critical issues is the selection and design of expanders.

As the energy output component, the form, efficiency, and reliability of the expander greatly affect the efficiency and technical economy of the ORC systems. At present, the expanders applied to ORC system are mainly divided into velocity-type and volume-type expanders [13]. Velocity-type expanders, also known as turbo expanders, mainly include axial flow turbines and radial flow turbines [14, 15]. The principle is to convert the heat energy from high temperature and pressure gas to kinetic energy, then driving the system to operate. Velocity-type expanders are often used in large-flow and high-power ORC systems, which have mature manufacturing processes, simple structures, and long service life. However, they have relatively high rotational speeds and mechanical losses. Volume-type expanders are mainly divided into scroll expanders, reciprocating piston expanders, screw expanders, and free piston expanders [16–18]. The principle is to obtain the output work of expansion ratio and enthalpy drop through volume change. Volume-type expanders have the characteristics of high expansion ratio and low speed, which are more suited for small-sized ORC systems. However, this type has higher requirements for lubrication and sealing [19].

Among these expanders, the free piston expander (FPE) offers more underlying advantages owing to the cancellation of the crank linkage mechanism and the reduction of moving components, which makes it promising for ORC systems to recover waste heat from automotive ICEs. The FPE was developed from the motor compressor apparatus proposed by the authors of [20], which eliminated the crank linkage mechanism of the reciprocating piston expander, allowing the piston to move freely within the cylinder. These features give it the advantages of compact structure, good sealability, low friction, high efficiency, and variable expansion ratio [21–24].

Heyl and Quack [25] designed the first generation of FPEs for $CO_2$ refrigeration cycles. Burugupally and Weiss [26, 27] reviewed the technical challenges, opportunities, and recent advances faced by FPEs. Meanwhile, they developed a physical model of a miniature FPE and investigated its operating characteristics and output performance. Weiss [28] designed a miniature FPE piezoelectric cantilever device applied to the low-temperature energy recovery system that transforms heat energy into electrical energy. Champagne and Weiss [29] investigated the influences of lubricant, inlet pressure, piston stroke, piston mass, and shape on the performance of small-scale FPE. The results displayed that thicker lubricants and low-viscosity lubricants provide better sealing performance in the experiments. Preetham and Weiss [30] established a nonlinear lumped-parameter model for a small-scale FPE and investigated the key factors affecting its operational performance. The results revealed that the piston mass, external load, and input heat have important effects on the operating frequency, output power, and thermal efficiency of the FPE.

In recent decades, a new type of free piston expander-linear generator (FPE-LG) has been developed, which directly couples the FPE with the LG. Kodakoglu [31] presented a single-piston two-chamber FPE-LG and optimized the sealing and expansion process of the expander. The results demonstrated that the FPE-LG prototype can achieve a maximum isentropic efficiency of 21.5% and generate a maximum actual expander work of 75.13 W. Ismael et al. [32, 33] developed a double-piston air-driven FPE-LG test rig and investigated the impacts of intake pressure and valve opening on piston motion, output power, and system stability. The results displayed that the FPE-LG can reach a maximum output power of 120 W when the valve opening duration is 30 ms and the intake pressure is 0.8 MPa. Wang et al. [34] carried out an experimental investigation of the dual-piston FPE-LG. The results displayed that the efficiency and working frequency of this FPE-LG increase as the driving pressure increases. The energy conversion efficiency can reach 55% when the driving pressure is 3.75 bar. Hou et al. [18, 24] developed an FPE-LG with the intake/exhaust valves controlled by servomotors and performed experimental studies. Based on the first generation, Hou et al. [35, 36] developed a new dual-piston FPE-LG using a tubular linear motor and electromagnetic valve distribution mechanism and established the ORC-FPE-LG combined system simulation model using Simulink and GT-Suite software. Tian et al. [37, 38] presented a single-piston FPE-LG for the small-sized ORC. The working principle of this FPE-LG and the impacts of intake and exhaust valve opening time on output characteristics were studied.

Currently, most simulation and experimental studies mainly focus on the working principle of the expander and the influence of operating parameters on its output performance. There are few studies on joint optimization of performance prediction and optimal output of FPE under full working conditions. On the one hand, it is difficult to accurately assess the optimal operational performance of an FPE using limited and dispersed data. On the other hand, experimental studies under full working conditions have the drawbacks of being time-consuming, susceptible to environmental influences and high cost. In theoretical research, assumptions are usually made on some parameters of FPE, which may lead to significant differences between the simulation result and the actual operating results. There is a nonlinear mapping relation between the working parameters of the FPE and its motion characteristics and output performance, which is difficult to analyze using traditional theoretical methods.

Advances in machine learning have given new ideas and methods for design and performance improvement in the field of ORC and expander systems. Among them, artificial neural networks (ANN) have been widely used due to their advantages in self-adaption, self-learning, nonlinear mapping, and fault tolerance [39–41]. Yang et al. [42] established an ANN prediction model for the diesel engine and ORC

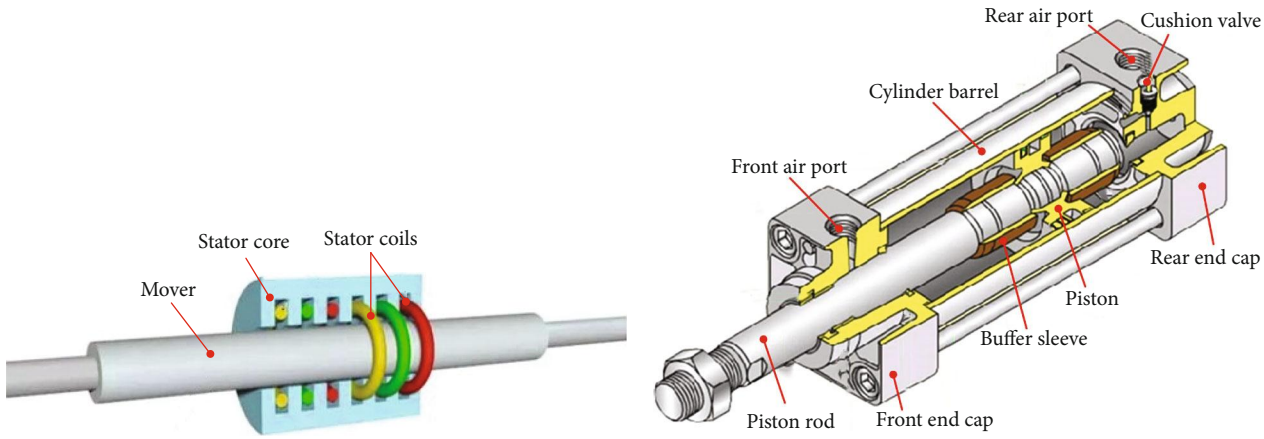


(a) Tubular PMLG (b) FPE

Figure 1: Structures of the SFPE-LG prototype.

system and investigated the influences of key working parameters on the output performance of entire system. Kim et al. [43] constructed a regression model based on ANN with two hidden layers to predict and optimize the performance of the radial flow turbine and ORC system. Palagi et al. [44] presented an ORC system optimization model on the basis of ANN and genetic algorithm, which combines the optimal selection of thermodynamic coefficients with the main design parameters for a radial flow turbine. Tian et al. [45] established a three-layer back propagation neural network-genetic algorithm model based on the correlation coefficient matrix for input and output variables.

The above literature review indicates that FPE-LGs are promising expansion machinery owing to their advantages in compact structure, low friction, and high efficiency. However, most published papers focus on basic principles and experimental studies of the FPE-LG prototype, especially for the single-piston free piston expander-linear generator (SFPE-LG). There are limited studies on the performance prediction of the SFPE-LG, and the optimal performance of the SFPE-LG under all operating conditions has not been studied in detail.

Moreover, conventional thermodynamic models do not perform well in predicting SFPE-LG characteristics and therefore cannot provide guidelines for improving output performance. In this paper, a back propagation neural network (BPNN) prediction model for the SFPE-LG was developed and verified based on the obtained experimental data under time and position control strategies. The influences of the model parameters such as the hidden layer, transfer function, training function, hidden layer nodes, and learning rate on the learning ability and predictive performance of this BPNN model were discussed. Based on the analysis results, the optimal model parameters were determined. Finally, an optimization model for the output power of the SFPE-LG was built by combining the genetic algorithm (GA) and BPNN model. The maximum output power and corresponding key working parameters of the SFPE-LG under different operation strategies were obtained.

Table 1: Basic parameters of the PMLG.

| Parameters | Values | Units |
|---|---|---|
| Thrust constant | 75 | N/A |
| Peak velocity | 3.5 | m/s |
| Peak thrust | 1500 | N |
| Induction | 40 | mH |
| Mover mass | 3.7 | kg |
| Peak current | 20 | A |

## 2. SFPE-LG Prototype and Test Bench

*2.1. Configuration of the SFPE-LG.* The LG plays a pivotal role in the SFPE-LG system as it significantly impacts the overall performance regarding power generation efficiency, rapid response times, and overall control. Generally, LGs can be classified into three types: permanent magnet linear generator (PMLG), linear induction generator, and linear switched reluctance generator [46]. Because of the advantages in high power density and efficiency, PMLGs are widely used in different systems that utilize the energy stored during the linear motion to convert to electricity. PMLGs can also be divided into the single-sided flat type, double-sided flat type, tubular type, and other special forms. Among these, the tubular PMLG is considered more efficient because it has higher power density per volume. Thus, a tubular PMLG was selected in this study. According to the different types of movers, tubular PMLGs can be divided into moving magnetic and moving coil types. The moving coil PMLG requires a guide wire to connect the windings and has a lower thrust density compared to the moving magnet type. Consequently, the moving magnetic tubular PMLG was adopted to match with the FPE. The main structure is displayed in Figure 1(a). The basic technical parameters are listed in Table 1.

Figure 1(b) presents the three-dimensional structures of this FPE, which comprises various parts such as the piston, buffer sleeve, piston rod, bearing, cushion valve, cylinder

barrel, air ports, sealing ring, and front and rear end caps. To reduce the mass of moving parts, the piston was made of forged aluminum alloy, the piston rod was made of high alloy steel, and the buffer sleeve was made of polyoxymethylene material. The buffer sleeves were processed on both sides of the piston to realize the self-buffering and anticollision functions. The main technical parameters of the FPE are listed in Table 2.

Figure 2 shows the SFPE-LG prototype, which was formed by connecting the piston and mover through the connecting rod. The only moving part of the SFPE-LG was called the piston mover assembly (PMA), which consisted of the piston, mover, piston rod, the bracket of the LG mover, and the connecting rod. The reading head of the grating displacement sensor was positioned on the PMA, and the grating ruler was installed on the platform to monitor the displacement of the PMA in real time. The cylinder of the FPE was split into two chambers by the piston, the right side of piston was defined as chamber A, and the left side of piston was defined as chamber B.

The position of the piston closest to the rear end cover in the FPE (the position where the piston is located when the volume of chamber A is 0) is defined as zero displacement. In a certain working cycle, when the piston moves to the minimum volume for chamber A, the position of the piston is defined as the top dead center (TDC). When the piston runs to the maximum volume for chamber A, the position of the piston is defined as the bottom dead center (BDC). Since the SFPE-LG is not limited by the crankshaft connecting rod mechanism, the TDC/BDC of the piston is uncertain. Thus, the actual stroke for the piston is also different under different working conditions. The distance between the TDC and BDC is defined as the actual stroke ($S_a$). When the position control strategy is adopted, there are two preset position points $P_1$ and $P_2$ at both ends of the FPE. The values of $P_1$ and $P_2$ can be freely adjusted according to different working conditions. The distance between $P_1$ and $P_2$ is defined as the preset stroke ($S_p$), expressed by $P_1 - P_2$ (mm) in the following text. The maximum stroke ($S_m$) of the piston is 70 mm.

*2.2. SFPE-LG Test Bench.* Figures 3 and 4 show the schematic and physical diagrams of the SFPE-LG test bench, which mainly consists of the SFPE-LG prototype, an air compressor, a dryer, a filter, a pressure regulator, two flowmeters, four solenoid valves, sliding rheostat, acquisition controller, computer, rectifier circuit, and various sensors. The air compressor is adopted to provide high-pressure gas, and the dryer and filter are used to remove moisture and impurities in the high-pressure gas. The pressure regulator is adopted to regulate the gas pressure entering the FPE. The electrical energy produced by the LG is consumed by the sliding rheostat after being processed by the rectifier circuit. The collected information mainly includes the cylinder pressure, intake and exhaust temperature, flow rate, displacement of the PMA, output voltage, current, and power. The acquisition controller controls the opening and closing of the solenoid valves according to the collected information, thus realizing the stable running of the SFPE-LG. The detailed introduction and working principle of the SFPE-LG can be found in our previous papers [47, 48].

Table 2: Basic parameters of the FPE.

| Parameters | Value | Unit |
|---|---|---|
| Piston mass | 0.32 | kg |
| Piston rod diameter | 16 | mm |
| Working pressure | 0 ~ 1.2 | MPa |
| Maximal stroke | 70 | mm |
| Cylinder bore | 40 | mm |
| Working temperature | -20~80 | ˚C |

*2.3. Operation Strategy.* Since the SFPE-LG abandons the crank linkage mechanism, the movement of PMA has sufficient "freedom," and the TDC/BDC may change under different working cycles. Therefore, precise control for the motion of PMA is a challenge for such SFPE-LGs. The control target is to keep a stable operation and prevent collisions between the piston and end cap. Moreover, the intake and exhaust timing control strategies should maximize the output power and energy conversion efficiency of SFPE-LG. On the basis of the existing valve distribution system and LabVIEW software, two sets of intake and exhaust timing control strategies were proposed, time control strategy (TCS) and position control strategy (PCS), both of which realized stable operation of the SFPE-LG prototype. In conjunction with Figure 3, the working process is described in detail as follows.

*Time control strategy*: when the SFPE-LG starts to work, solenoid valves V1 and V4 are opened, and V3 and V2 are closed. The high-pressure gas flows into chamber A through the rear air port and pushes the piston to begin moving from TDC to BDC. After intake duration $t_{in}$, solenoid valve V1 is closed and other solenoid valves remain unchanged. The high-pressure gas expands freely in chamber A and continues to push the piston. The exhaust gas in chamber B flows out through the front air port. After expansion duration $t_{ex}$, solenoid valves V2 and V3 are opened, and V1 and V4 are closed. The high-pressure gas flows into chamber B through the front air port and pushes the piston to begin moving from BDC to TDC. After intake duration $t_{in}$, solenoid valve V2 is closed and other solenoid valves remain invariable. The high-pressure gas expands freely in chamber B and continues to drive the piston. After expansion duration $t_{ex}$, solenoid valves V1 and V4 are opened, V3 and V2 are closed, and the next working cycle starts.

*Position control strategy*: when the SFPE-LG starts to operate, solenoid valves V1 and V4 are opened, and V3 and V2 are closed. The high-pressure gas flows into chamber A through the rear air port, and the piston starts to move from its TDC to BDC. After intake duration $t_{in}$, solenoid valve V1 is closed and other solenoid valves remain unchanged. The high-pressure gas expands freely in chamber A and continues to push the piston. When the piston reaches the preset position point $P_2$, solenoid valves V2

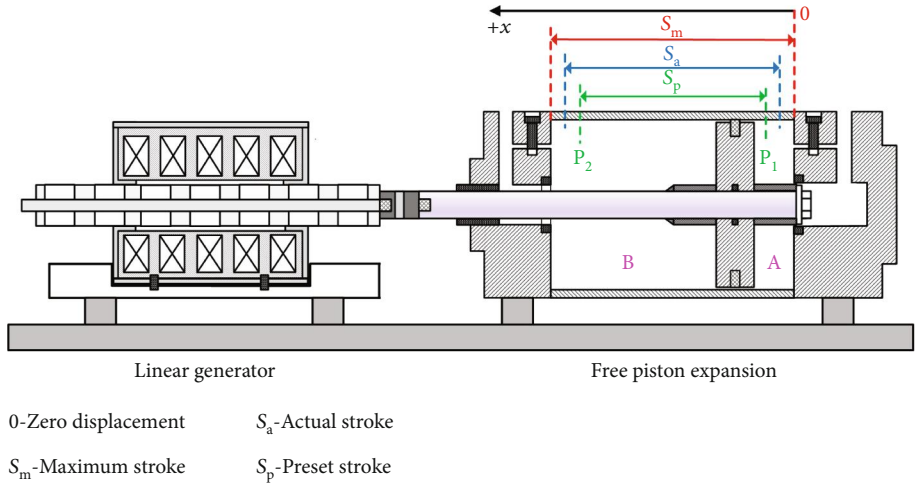


Figure 2: Diagram of the SFPE-LG prototype.

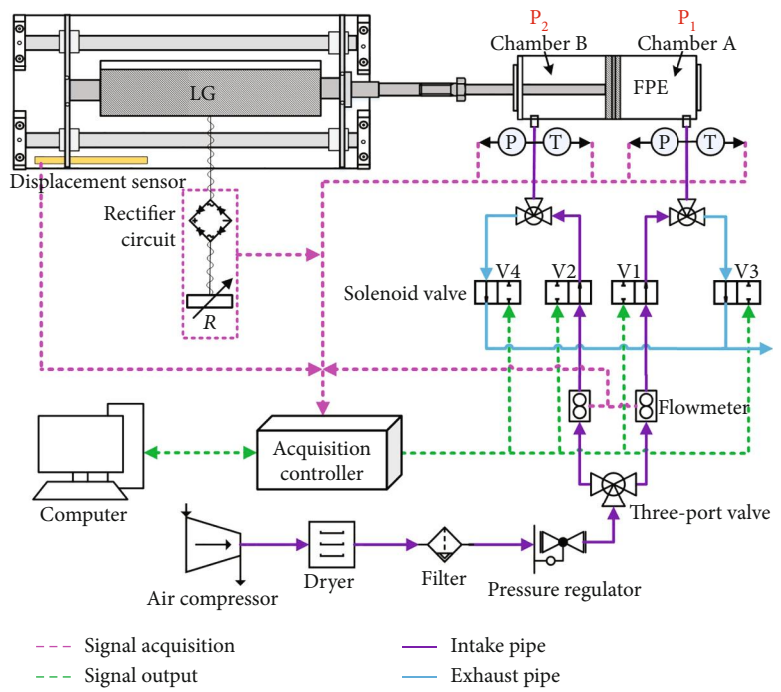


Figure 3: Schematic of the SFPE-LG test bench.

and V3 are opened, and V1 and V4 are closed. The high-pressure gas starts to flow into chamber B and then drives the piston to move from its BDC to TDC. Similarly, after intake duration $t_{in}$, solenoid valve V2 is closed and other solenoid valves remain invariable. The high-pressure gas expands freely in chamber B and continues to drive the piston. When the piston reaches the preset position point $P_1$, solenoid valves V1 and V4 are opened, V3 and V2 are closed, and the next working cycle starts.

## 3. Prediction Model and Parameter Analysis

The ANNs are the mathematical models that imitate the behavioral characteristics of animal neural networks for distributed parallel information processing. The ANNs have self-learning and self-adaptive capabilities, which can analyze and grasp the potential laws between the corresponding input and output data provided in advance. Based on the obtained laws, the desired output results can be predicted according to the input data. Similar to the biological nervous systems, the ANNs are also composed of artificial neurons as the basic units. Each neuron of the ANN stands for a specific function, that is, the activation function. The connection between every two neurons provides the memory of ANN and is represented by the weights. Therefore, the output results of this ANN model vary depending on the connection methods, weight values, and activation functions.

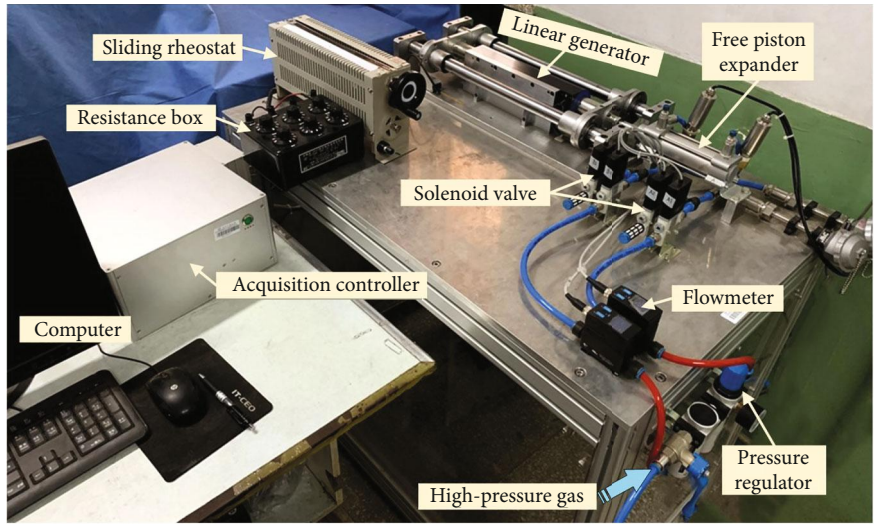


Figure 4: Physical map of the SFPE-LG test bench.

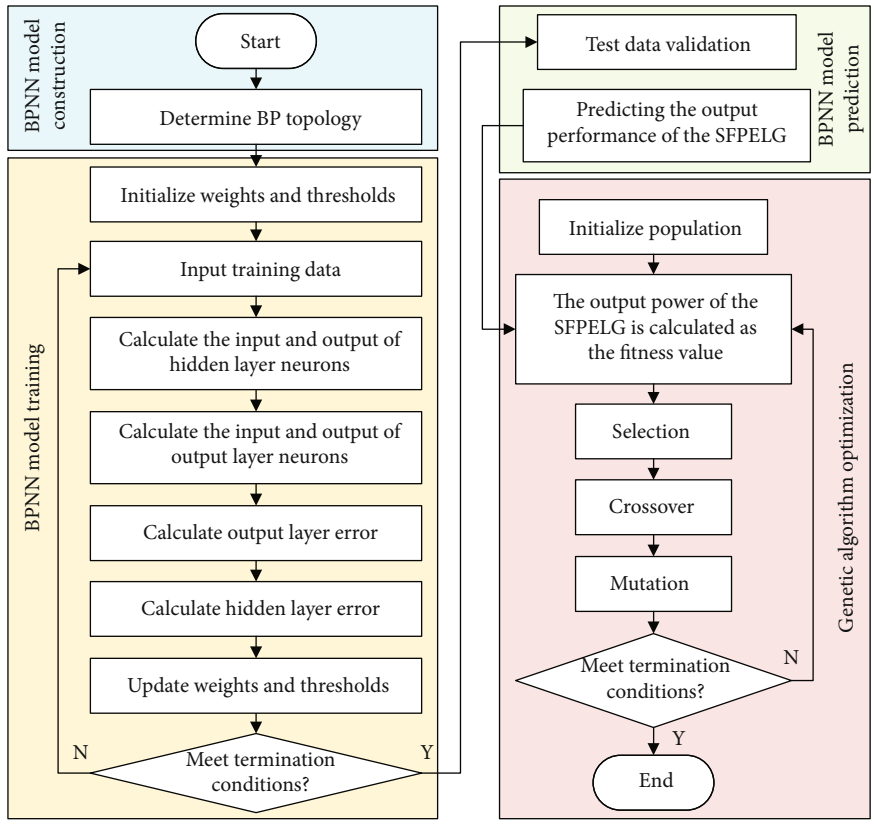


Figure 5: Flow chart of the BPNN model combined with GA for the SFPE-LG.

Among many ANNs, BPNN has attracted much attention due to its clear physical concepts, solid theoretical foundation, and good adaptability. BPNN is a multilayer forward neural network that includes an input layer, one or more hidden layers, and an output layer. These layers are fully interconnected, while the same layers are not connected to each other. The fundamental principle of BPNN divides into two procedures: the forward propagation from the input layer to the output layer is adopted to analyze the error, and the back propagation from the output layer to the input layer is used to change the weights and biases. After extensive learning and training, the BPNN model stops iterating and determines the optimum weights and biases when the errors achieve the expected values.

GA is a parallel random search optimization method inspired by natural genetic mechanisms and biological evolution. This algorithm is used to achieve the optimum

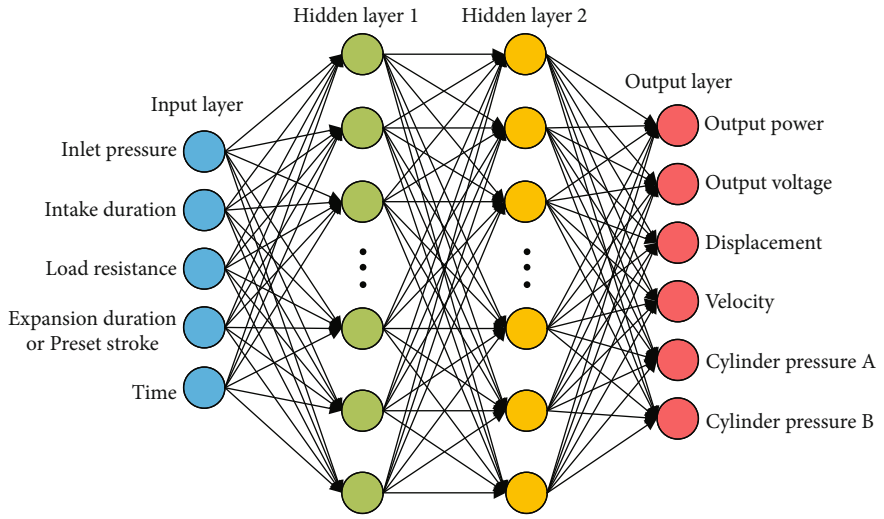


Figure 6: The BPNN topology of the SFPE-LG.

solution for an optimization problem. Evolution is an iterative process, and the first generation is generated randomly. The fitness function in each generation is evaluated. The evolution process will stop when the maximum number of generations or satisfactory fitness is achieved. To make up for the shortcomings in experimental and simulation studies, the BPNN model was coupled with the GA to establish a nonlinear relationship between the output performance and working parameters of SFPE-LG, thereby predicting and optimizing the maximum output power of SFPE-LG under all working conditions.

*3.1. BPNN Model Construction.* Figure 5 shows the flow chart of the performance prediction and optimization calculation for the SFPE-LG using the BPNN model and GA. Firstly, the performance prediction model of SFPE-LG was constructed according to the experimental data. Secondly, the effects of different factors on the predictive ability were investigated. The optimal parameter settings for the BPNN model were determined. Then, the established BPNN model was trained until the error requirement was satisfied. Finally, the prediction model was coupled to a GA for predicting and optimizing the maximum output power of the SFPE-LG at full working conditions.

The stable operation and maximum output power of the SFPE-LG involve the synergistic changes of multiple operating parameters. When the SFPE-LG operated at TCS, five key operating parameters, including inlet pressure, intake duration, load resistance, expansion duration, and running time, were chosen as the input variables of this BPNN model. When the SFPE-LG run at PCS, five key operating parameters, including intake duration, inlet pressure, load resistance, preset stroke, and running time, were used as the input variables of this BPNN model. In these two control strategies, six key output parameters such as cylinder pressure in chambers A and B, output power, output voltage, displacement, and velocity of the PMA, were selected as output layer variables.

For the hidden layer, there is no widely recognized method for selecting its number of layers. Researchers need to determine different network structures for specific research problems [49, 50]. Based on the preliminary trial calculations and comprehensive consideration of prediction accuracy and training time, two hidden layers were selected in this study. Furthermore, there is also no unified method to determine the optimal number of hidden layer nodes, so the effects of hidden layer nodes number on the predictive ability of this BPNN model were explored. To simplify this calculation, the number of nodes in both hidden layers was set to be the same. Finally, the established BPNN topology of the SFPE-LG is displayed in Figure 6.

*3.2. Model Evaluation Criteria.* In this study, six commonly used indicators were selected to evaluate the training and prediction accuracy of the established BPNN model. These indicators include the mean square error (MSE), root mean square error (RMSE), mean absolute error (MAE), root mean absolute error (RMAE), mean absolute percentage error (MAPE), and correlation coefficient ($R$). The mathematical expressions for these indicators are represented by the following equations [51, 52].

$$\begin{aligned}
\mathrm{MSE} &= \frac{1}{N}\sum_{i=1}^{N}[y_i-\hat{y}_i]^2,\\
\mathrm{RMSE} &= \sqrt{\frac{1}{N}\sum_{i=1}^{N}[y_i-\hat{y}_i]^2},\\
\mathrm{MAE} &= \frac{1}{N}\sum_{i=1}^{N}|y_i-\hat{y}_i|,\\
\mathrm{RMAE} &= \sqrt{\frac{1}{N}\sum_{i=1}^{N}|y_i-\hat{y}_i|},\\
\mathrm{MAPE} &= \frac{1}{N}\sum_{i=1}^{N}\left|\frac{y_i-\hat{y}_i}{y_i}\right|\cdot 100\%,\\
R &= \frac{(y_i-\bar{y})(\hat{y}_i-\bar{\hat{y}})^{\mathrm{T}}}{\sqrt{(y_i-\bar{y})(y_i-\bar{y})^{\mathrm{T}}}\sqrt{(\hat{y}_i-\bar{\hat{y}})(\hat{y}_i-\bar{\hat{y}})^{\mathrm{T}}}},
\end{aligned} \tag{1}$$

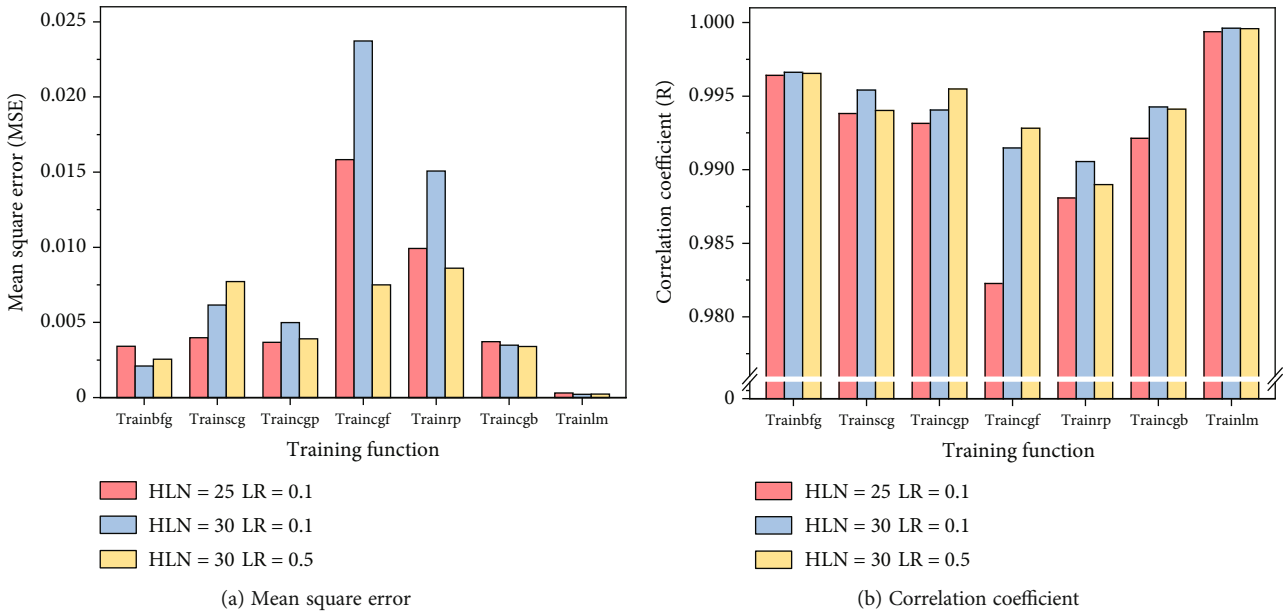


(a) Mean square error

(b) Correlation coefficient

Figure 7: The influences of training function on BPNN model under the TCS.

where $N$ represents the sample number, $y_i$ signifies the predictive results of the BPNN model, $\hat{y}_i$ is the experimental result, $\bar{y}$ indicates the average value of the prediction results, and $\bar{\hat{y}}$ signifies the average value of the experimental result.

The smaller the MSE and RMSE values, the smaller the fluctuation in the error vector and the more stable the output results. The smaller the MAE, RMAE, and MAPE values are, the smaller the difference between the predictive results and the experimental results is, indicating better prediction performance. The correlation coefficient indicates the degree of linear correlation between the predictive results and experimental results, and its value closer to one is better.

*3.3. Transfer Function.* The transfer function (activation function) is an important part of this BPNN model. The selection of transfer function includes the selection of hidden layer function and output layer function. The hidden layers usually use a sigmoid function as the transfer function, while the output layer usually uses the linear transfer function, that is, purelin function. The sigmoid transfer function has two functions, the logsig function and the tansig function, which can map the training data to intervals [0, 1] and [-1, 1], respectively [53].

$$\begin{aligned} \text{Logsig function} &: y = \frac{1}{1+e^{-x}}, \\ \text{Tansig function} &: y = \frac{2}{1+e^{-2x}} - 1, \\ \text{Purelin function} &: y = x. \end{aligned} \tag{2}$$

The transfer function should be selected according to the specific situation in practical applications. Generally, this choice mainly depends on the relationship between the input and output data. If the output values do not contain negative values, the BPNN model can adopt the logsig function. If the output values contain some negative values, the tansig function can be used for the transfer function. In the training data samples selected in this study, a portion of the output values for the piston velocity was negative. Therefore, the tansig function was selected as the transfer function for the hidden layer in the proposed BPNN model. The purelin function was selected as the transfer function for the output layer.

*3.4. Training Function.* Many types of training functions can be applied to BPNN models, and different training functions have their advantages and disadvantages. Thus, it is difficult to choose a suitable training function for the BPNN model without comparative screening. In this section, the impact of the training function on MSE and correlation coefficient under these two control strategies is investigated, as shown in Figures 7 and 8. Seven training functions are selected for the BPNN model of SFPE-LG, as follows: trainbfg, trainscg, traincgp, traincgf, trainrp, traincgb, and trainlm.

Trainbfg is a training function for the BFGS quasi Newton algorithm, which requires relatively few iterations and has a fast convergence speed. Traincgf, traincgp, traincgb, and trainscg are four conjugate gradient algorithm functions. Traincgf is a Fletcher-Reeves conjugate gradient algorithm function with minimal storage requirements. Traincgp is a function of the Polak-Ribiere conjugate gradient algorithm. Traincgb is the Powell-Beale conjugate gradient algorithm function, which determines whether the adjustment direction of the weights and thresholds returns to the negative gradient direction based on the orthogonality of the front and rear gradients. Trainscg represents the proportional conjugate gradient algorithm that does not need to compute the research direction. Trainrp is an elastic gradient descent algorithm function, which can eliminate the influence of gradient modulus on network training and improve

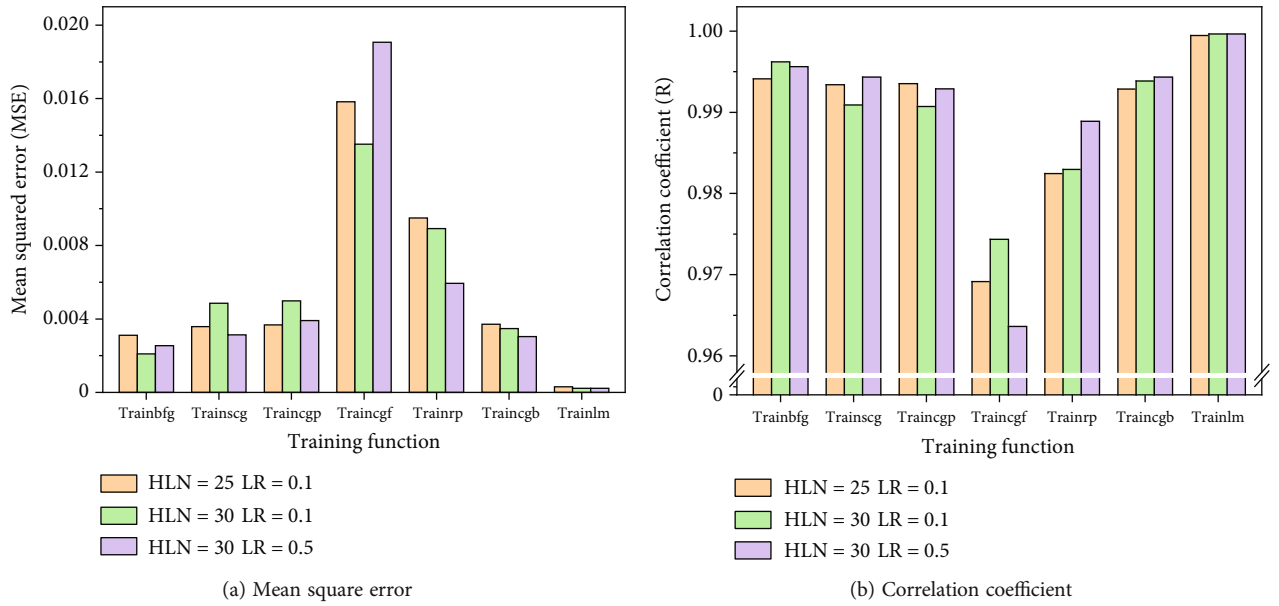


(a) Mean square error

(b) Correlation coefficient

Figure 8: The influences of training function on BPNN model under the PCS.

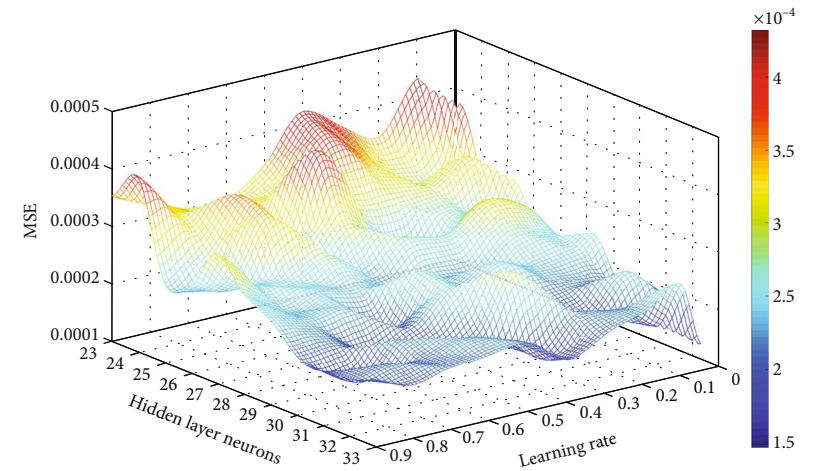


(a) Effects of HLN and LR on mean square error

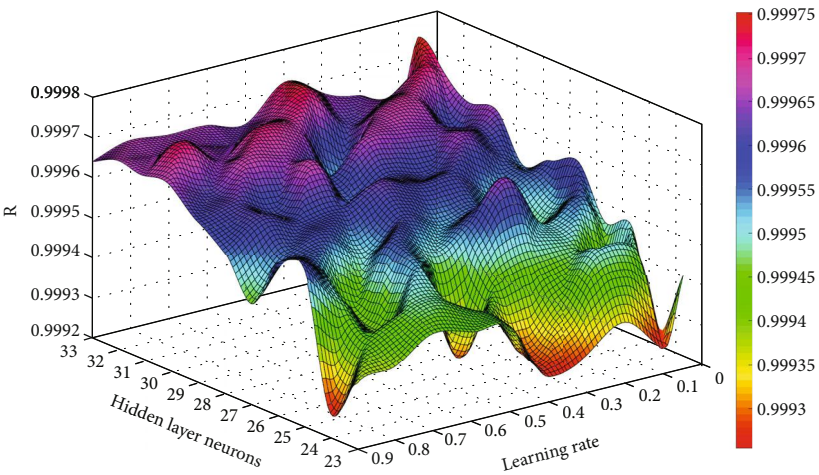


(b) Effects of HLN and LR on correlation coefficient

Figure 9: Effects of HLN and LR on prediction accuracy under the TCS.

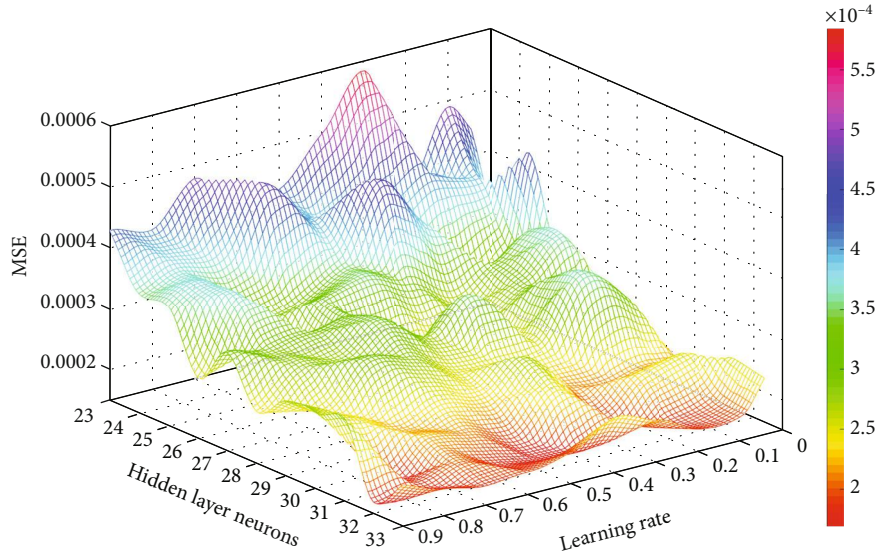


(a) Effects of HLN and LR on mean square error

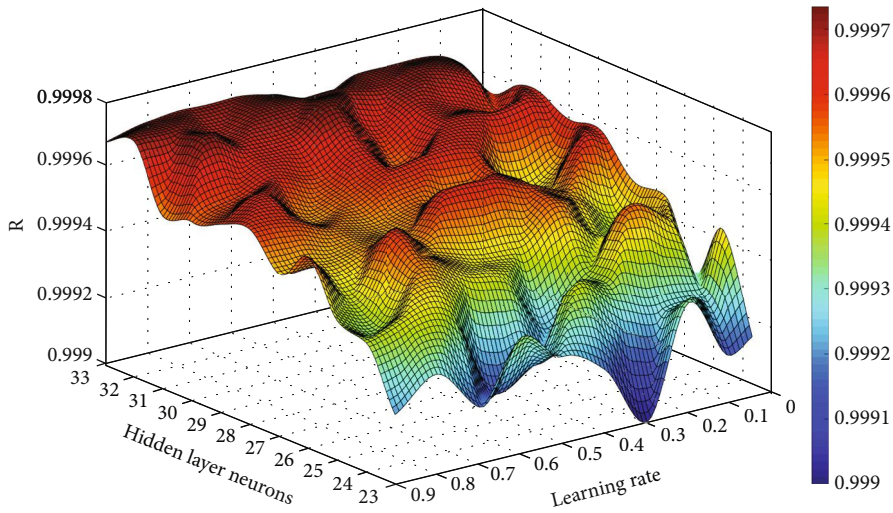


(b) Effects of HLN and LR on correlation coefficient

Figure 10: Effects of HLN and LR on prediction accuracy under the PCS.

Table 3: Parameters of the BPNN model for SFPE-LG.

| Items | Values |
|---|---|
| Training function | Trainlm |
| Input variables | 5 |
| Transfer function for hidden layer | Tansig |
| Learning rate | 0.4 |
| Transfer function for output layer | Purelin |
| Maximum training times | 1000 |
| Number of hidden layers | 2 |
| Output variables | 6 |
| Training target accuracy | $10^{-4}$ |
| Number of hidden layer nodes | 32 |

training speed. Trainlm represents the Levenberg-Marquardt optimization algorithm, which is the most commonly adopted training function in BPNN models.

It can be seen from Figures 7 and 8 that this BPNN model has the highest predictive accuracy when the trainlm was chosen as the training function at different hidden layer node (HLN) numbers and learning rates (LR). The worst model prediction accuracy was obtained by traincgf. When the number of HLN was 30 and the LR was 0.5, the BPNN model of SFPE-LG achieved the minimum MSE of $2.282 \times 10^{-4}$ and the maximum correlation coefficient of 0.9997. Therefore, trainlm was adopted as the training function under both time and position control strategies.

*3.5. Hidden Layer Nodes and Learning Rate.* In the BPNN model, the number of nodes for this input and output layers is determined, while the number of HLN is unknown. However, the number of HLN is a critical

Table 4: Experimental conditions of SFPE-LG prototype used for model prediction and validation.

| No. | Inlet pressure (MPa) | Intake duration (ms) | Load resistance (Ω) | Expansion duration (ms) | Preset stroke (mm) |
|---|---|---|---|---|---|
| 1 | 0.3 | 15 | 50 | 70 | 0 |
| 2 | 0.4 | 20 | 70 | 90 | 0 |
| 3 | 0.5 | 25 | 90 | 105 | 0 |
| 4 | 0.6 | 30 | 110 | 120 | 0 |
| 5 | 0.7 | 15 | 70 | 120 | 0 |
| 6 | 0.3 | 20 | 50 | 105 | 0 |
| 7 | 0.4 | 25 | 110 | 90 | 0 |
| 8 | 0.5 | 30 | 90 | 70 | 0 |
| 9 | 0.6 | 15 | 110 | 70 | 0 |
| 10 | 0.7 | 20 | 50 | 120 | 0 |
| 11 | 0.4 | 20 | 40 | 0 | 10-60 |
| 12 | 0.4 | 25 | 60 | 0 | 15-55 |
| 13 | 0.5 | 30 | 80 | 0 | 20-50 |
| 14 | 0.5 | 35 | 100 | 0 | 15-55 |
| 15 | 0.6 | 20 | 100 | 0 | 10-60 |
| 16 | 0.6 | 25 | 80 | 0 | 20-50 |
| 17 | 0.7 | 30 | 60 | 0 | 20-50 |
| 18 | 0.7 | 35 | 40 | 0 | 15-55 |
| 19 | 0.4 | 20 | 80 | 0 | 10-60 |
| 20 | 0.5 | 25 | 100 | 0 | 15-55 |
| … | … | … | … | … | … |

parameter among the many parameters of the BPNN model, which has a significant influence on the prediction performance. A small number of HLN will reduce the learning ability of this BPNN model, which is insufficient to establish the nonlinear mapping regulations involved in the experimental data. A large number of HLN will not only increase the learning time of this model but also lead to overfitting problems, thereby reducing the generalization ability of this BPNN model. Currently, there are no scientific rules to determine the number of HLN. Generally, the initial value of the HLN number is obtained according to an empirical formula, and then, the number of nodes is gradually increased or decreased based on this value to compare the predictive performance of each BPNN model. Finally, few nodes as possible are selected as the number of HLN for this BPNN model under the premise of satisfying the predictive accuracy.

In the BPNN model, another important parameter is the learning rate, which indicates the magnitude of the change for the weight coefficient generated in each cycle. The larger the learning rate value, the greater the weight change and the faster the convergence speed. If the LR is too large, it will cause the model to oscillate or fail to converge. If the LR is small, the convergence speed will be slowed down, but it can prevent the BPNN model from falling into local convergence, and the model will eventually tend to the minimum error. Therefore, to ensure the stability and predictive ability of this BPNN model, a small learning rate should be selected, typically between 0.01 and 0.7.

Figure 9 depicts the effects of HLN number and LR on the predictive accuracy of this BPNN model under the TCS. The results show that as the number of hidden layer nodes increases from 23 to 33 with an interval of 1 and the LR changes from 0.9 to 0.05, the MSE of the BPNN model gradually decreases, and the correlation coefficient gradually increases and approaches 1. These indicate that the predictive performance of the proposed BPNN mode is getting better gradually. Generally, a smaller MSE corresponds to a higher correlation coefficient, and the effects of the number for HLN on the MSE and correlation coefficient are more significant than that of the learning rate. When the number of HLN is greater than 30, no matter how the learning rate changes, the BPNN model of SFPE-LG always has a very low MSE and a high correlation coefficient. When HLN = 31 and LR = 0.8, or HLN = 32 and LR = 0.1, or HLN = 32 and LR = 0.4, the MSE of the BPNN model gets the minimum value of 0.000167, and the correlation coefficient achieves the maximum value of 0.99972.

Figure 10 demonstrates the effects of HLN number and LR on the predictive accuracy of this BPNN model under the PCS. When the SFPE-LG operates at the PCS, the training results are similar to those of the TCS. When the number of hidden layer nodes increases from 23 to 33 and the learning rate changes from 0.9 to 0.05, the MSE of the BPNN model gradually decreases, and the correlation coefficient gradually increases. This shows that the prediction performance of the proposed BPNN model is gradually improving. When HLN = 32 and LR = 0.4 or HLN = 32 and LR = 0.5, the MSE of the BPNN model has a minimum value of 0.00017, and the correlation coefficient has a maximum value of 0.99971. These working cases suggest that the

Table 5: Fivefold cross-validation results under the TCS.

| Fivefold results | Parameters | MSE | RMSE | MAE | RMAE | MAPE | $R$ |
|---|---|---|---|---|---|---|---|
| First | Cylinder pressure A | 0.0019 | 0.0431 | 0.0240 | 0.1550 | 1.29% | 0.9958 |
| | Cylinder pressure B | 0.0012 | 0.0345 | 0.0234 | 0.1530 | 1.20% | 0.9982 |
| | Displacement | 0.1034 | 0.3216 | 0.2533 | 0.5033 | 0.68% | 0.9994 |
| | Voltage | 0.3556 | 0.5963 | 0.4550 | 0.6745 | 2.75% | 0.9970 |
| | Power | 0.1484 | 0.3853 | 0.2914 | 0.5398 | 23.41% | 0.9983 |
| | Velocity | 0.0001 | 0.0097 | 0.0070 | 0.0835 | 0.78% | 0.9992 |
| Second | Cylinder pressure A | 0.0016 | 0.0395 | 0.0224 | 0.1498 | 1.15% | 0.9967 |
| | Cylinder pressure B | 0.0015 | 0.0389 | 0.0248 | 0.1574 | 1.28% | 0.9977 |
| | Displacement | 0.0898 | 0.2996 | 0.2356 | 0.4854 | 0.64% | 0.9995 |
| | Voltage | 0.3495 | 0.5912 | 0.4339 | 0.6587 | 2.87% | 0.9973 |
| | Power | 0.1327 | 0.3643 | 0.2780 | 0.5272 | 12.26% | 0.9987 |
| | Velocity | 0.0001 | 0.0092 | 0.0071 | 0.0840 | 8.19% | 0.9993 |
| Third | Cylinder pressure A | 0.0022 | 0.0472 | 0.0240 | 0.1548 | 1.21% | 0.9955 |
| | Cylinder pressure B | 0.0017 | 0.0416 | 0.0234 | 0.1531 | 1.20% | 0.9974 |
| | Displacement | 0.0926 | 0.3044 | 0.2417 | 0.4916 | 0.66% | 0.9994 |
| | Voltage | 0.3848 | 0.6204 | 0.4681 | 0.6842 | 3.00% | 0.9970 |
| | Power | 0.1630 | 0.4037 | 0.3059 | 0.5530 | 1.57% | 0.9984 |
| | Velocity | 0.0001 | 0.0087 | 0.0066 | 0.0811 | 4.15% | 0.9993 |
| Fourth | Cylinder pressure A | 0.0013 | 0.0356 | 0.0197 | 0.1404 | 1.06% | 0.9972 |
| | Cylinder pressure B | 0.0012 | 0.0345 | 0.0220 | 0.1484 | 1.13% | 0.9981 |
| | Displacement | 0.0847 | 0.2911 | 0.2255 | 0.4749 | 0.60% | 0.9995 |
| | Voltage | 0.3270 | 0.5719 | 0.4389 | 0.6625 | 2.99% | 0.9974 |
| | Power | 0.1264 | 0.3556 | 0.2729 | 0.5224 | 11.27% | 0.9987 |
| | Velocity | 0.0001 | 0.0091 | 0.0069 | 0.0830 | 9.39% | 0.9993 |
| Fifth | Cylinder pressure A | 0.0016 | 0.0399 | 0.0214 | 0.1462 | 1.13% | 0.9965 |
| | Cylinder pressure B | 0.0017 | 0.0417 | 0.0258 | 0.1608 | 1.25% | 0.9977 |
| | Displacement | 0.0879 | 0.2964 | 0.2280 | 0.4775 | 0.60% | 0.9995 |
| | Voltage | 0.3474 | 0.5894 | 0.4566 | 0.6757 | 2.93% | 0.9970 |
| | Power | 0.1609 | 0.4012 | 0.3006 | 0.5483 | 10.79% | 0.9982 |
| | Velocity | 0.0001 | 0.0099 | 0.0071 | 0.0841 | 4.76% | 0.9991 |

established BPNN model of SFPE-LG has high accuracy in predicting the experimental data.

To sum up, the number of hidden layer nodes and the learning rate for the BPNN model of SFPE-LG are uniformly set to 32 and 0.4. In this way, the BPNN model has high prediction accuracy under both control strategies. Table 3 lists the detailed parameters of the established BPNN model, and the remaining parameters not listed adopt the default values.

## 4. Results and Discussion

*4.1. Training Accuracy of the BPNN Model.* Before using this established BPNN model to predict and optimize the performance of SFPE-LG, its training and prediction accuracy need to be verified. The S-fold cross-validation algorithm randomly divides the dataset into $S$ disjoint subsets, where the ($S$-1) subsets are called the training set, and the remaining one subset is called the validation set. During the model training process, the training set is used to train the model, and then, the validation set is used to verify the trained model. Among the $S$ subsets, each subset will be selected as validation data for the above training process. In this study, 5-fold cross-validation was chosen to check the robustness of the BPNN model.

The data used for the training, validation, and testing of the BPNN were obtained from the experimental platform shown in Figure 4, and some specific experimental conditions are shown in Table 4. When the SFPE-LG adopts the TCS, 6455 data points were selected and randomly divided into 5 datasets, 4 datasets of which were used to train the BPNN model, and the remaining one dataset (1291 data points) was adopted to verify the training accuracy of the BPNN model. Under the PCS, 6195 data points were selected and randomly divided into 5 datasets, 4 datasets of which were used to train the BPNN model, and the remaining one dataset (1239 data points) was used to verify the training accuracy of the BPNN model. The training error during $S$ training process is evaluated, and the model with

Table 6: Fivefold cross-validation results under the PCS.

| Fivefold results | Parameters | MSE | RMSE | MAE | RMAE | MAPE | $R$ |
|---|---|---|---|---|---|---|---|
| First | Cylinder pressure A | 0.0014 | 0.0380 | 0.0209 | 0.1445 | 1.02% | 0.9978 |
| | Cylinder pressure B | 0.0016 | 0.0396 | 0.0244 | 0.1562 | 1.12% | 0.9980 |
| | Displacement | 0.0615 | 0.2479 | 0.1875 | 0.4330 | 0.74% | 0.9997 |
| | Voltage | 0.4629 | 0.6803 | 0.5317 | 0.7292 | 2.43% | 0.9985 |
| | Power | 0.1769 | 0.4205 | 0.2947 | 0.5429 | 8.13% | 0.9989 |
| | Velocity | 0.0001 | 0.0100 | 0.0074 | 0.0860 | 0.42% | 0.9995 |
| Second | Cylinder pressure A | 0.0016 | 0.0398 | 0.0257 | 0.1602 | 1.30% | 0.9975 |
| | Cylinder pressure B | 0.0029 | 0.0542 | 0.0330 | 0.1816 | 1.70% | 0.9964 |
| | Displacement | 0.0531 | 0.2303 | 0.1776 | 0.4214 | 0.69% | 0.9998 |
| | Voltage | 0.5800 | 0.7616 | 0.5878 | 0.7667 | 2.80% | 0.9983 |
| | Power | 0.1516 | 0.3894 | 0.2865 | 0.5353 | 3.75% | 0.9991 |
| | Velocity | 0.0001 | 0.0098 | 0.0072 | 0.0848 | 0.68% | 0.9995 |
| Third | Cylinder pressure A | 0.0040 | 0.0633 | 0.0281 | 0.1677 | 1.38% | 0.9940 |
| | Cylinder pressure B | 0.0030 | 0.0548 | 0.0333 | 0.1824 | 1.65% | 0.9963 |
| | Displacement | 0.1062 | 0.3258 | 0.2297 | 0.4793 | 0.89% | 0.9996 |
| | Voltage | 0.9066 | 0.9521 | 0.6614 | 0.8132 | 2.99% | 0.9972 |
| | Power | 0.2686 | 0.5182 | 0.3459 | 0.5881 | 1.21% | 0.9984 |
| | Velocity | 0.0002 | 0.0139 | 0.0089 | 0.0946 | 5.12% | 0.9990 |
| Fourth | Cylinder pressure A | 0.0018 | 0.0422 | 0.0230 | 0.1518 | 1.17% | 0.9972 |
| | Cylinder pressure B | 0.0022 | 0.0464 | 0.0297 | 0.1724 | 1.48% | 0.9975 |
| | Displacement | 0.0526 | 0.2294 | 0.1774 | 0.4212 | 0.69% | 0.9998 |
| | Voltage | 0.5867 | 0.7660 | 0.5735 | 0.7573 | 2.54% | 0.9982 |
| | Power | 0.2121 | 0.4606 | 0.3289 | 0.5735 | 12.6% | 0.9987 |
| | Velocity | 0.0001 | 0.0104 | 0.0078 | 0.0886 | 0.25% | 0.9994 |
| Fifth | Cylinder pressure A | 0.0026 | 0.0513 | 0.0269 | 0.1641 | 1.34% | 0.9961 |
| | Cylinder pressure B | 0.0028 | 0.0533 | 0.0321 | 0.1793 | 1.53% | 0.9968 |
| | Displacement | 0.0688 | 0.2624 | 0.1978 | 0.4448 | 0.74% | 0.9997 |
| | Voltage | 0.6793 | 0.8242 | 0.5958 | 0.7719 | 2.72% | 0.9980 |
| | Power | 0.2937 | 0.5420 | 0.3839 | 0.6196 | 0.41% | 0.9983 |
| | Velocity | 0.0002 | 0.0133 | 0.0091 | 0.0954 | 1.48% | 0.9991 |

the smallest prediction error is selected. Finally, the prediction ability of the BPNN model was evaluated using the test set.

Table 5 shows the training accuracy of the BPNN model using 5-fold cross-validation under the TCS. The values of MSE and MAE with different folds are both small, and the correlation coefficient is close to 1. These results indicate that the trained BPNN model has a high prediction accuracy when the SFPE-LG is run under the TCS. Besides, the BPNN model has the best prediction accuracy at the fourth cross-validation. In the fourth training process, the correlation coefficients obtained from the linear regression analysis between the prediction and experimental results are 0.9972, 0.9981, 0.9995, 0.9974, 0.9987, and 0.9993 for the cylinder pressure in chamber A, cylinder pressure in chamber B, displacement of the PMA, output voltage, output power, and velocity of the PMA, respectively.

Table 6 shows the training accuracy of the BPNN model using 5-fold cross-validation under the PCS. In all cross-validation results, the values of MSE, RMSE, MAE, RMAE, and MAPE are very small, and the correlation coefficients are all close to 1. These results indicate that the established BPNN model of SFPE-LG has a high prediction accuracy when it runs at the PCS. The mean values of MAPE obtained from the 5-fold cross-validation are 1.24%, 1.50%, 0.75%, 2.70%, 5.22%, and 1.59% for the cylinder pressure of chamber A, cylinder pressure of chamber B, displacement of the PMA, output voltage, output power, and velocity of the PMA, respectively. Overall, the training results of the established BPNN model are in very high agreement with the experimental data under the two control strategies. In other words, the established BPNN model shows strong learning ability and generalization performance.

*4.2. Prediction Performance of the BPNN Model.* The established BPNN model is used to predict the operating performance of the SFPE-LG when operating at the TCS with an inlet pressure of 0.5 MPa, an intake duration of 30 ms, an

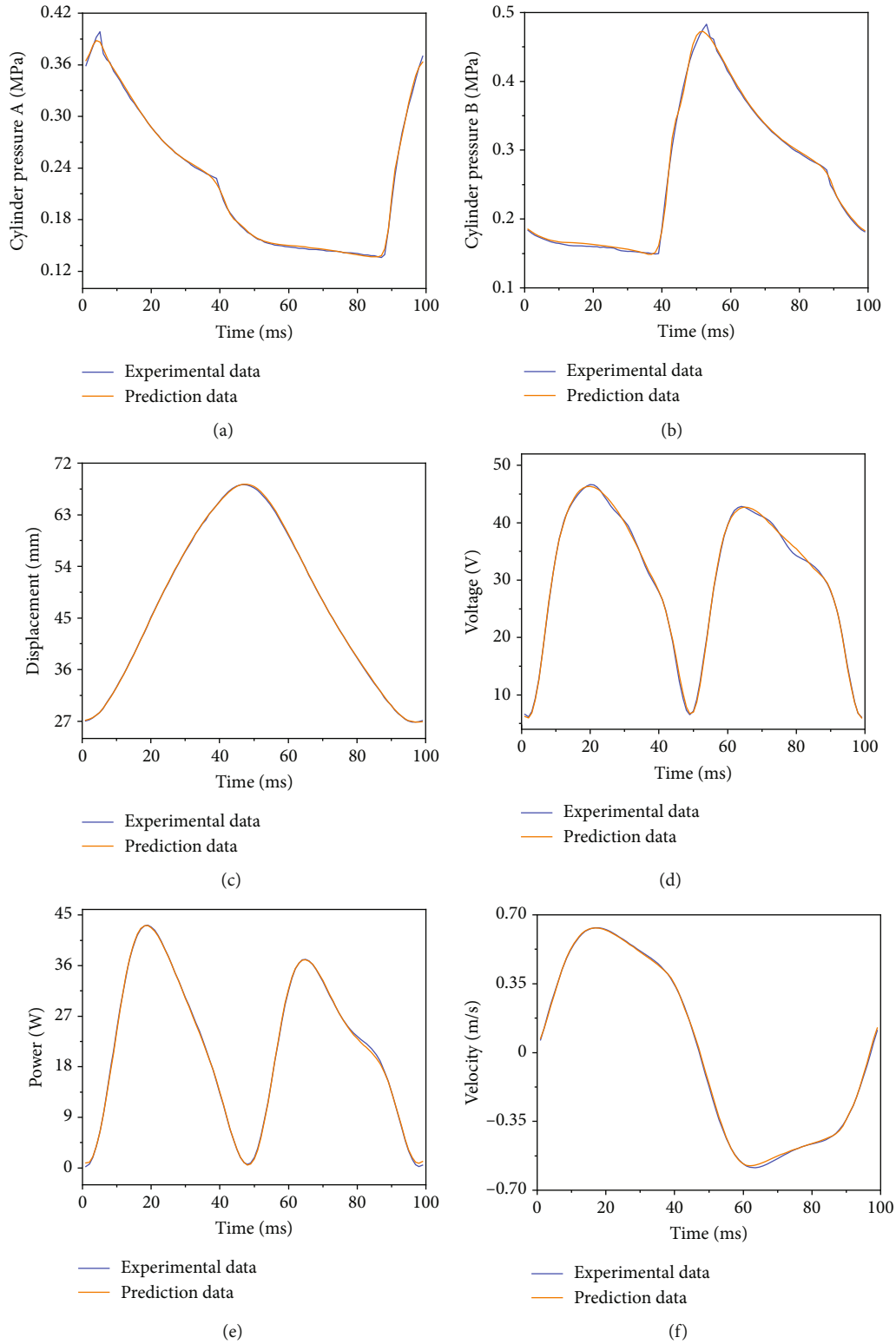


Figure 11: Comparison of experimental and prediction results under the TCS.

expansion duration of 70 ms, and a load resistance of 50 Ω. Figure 11 demonstrates the comparison of the prediction results with the experimental results for one working cycle. The comparison results show that the prediction curves of these six output variables are consistent with the experimental curves during one working cycle, and only obvious differences are found at some inflection points.

Figure 12 shows the absolute errors between the prediction and experimental results for the six output variables. The constructed BPNN model exhibits high prediction

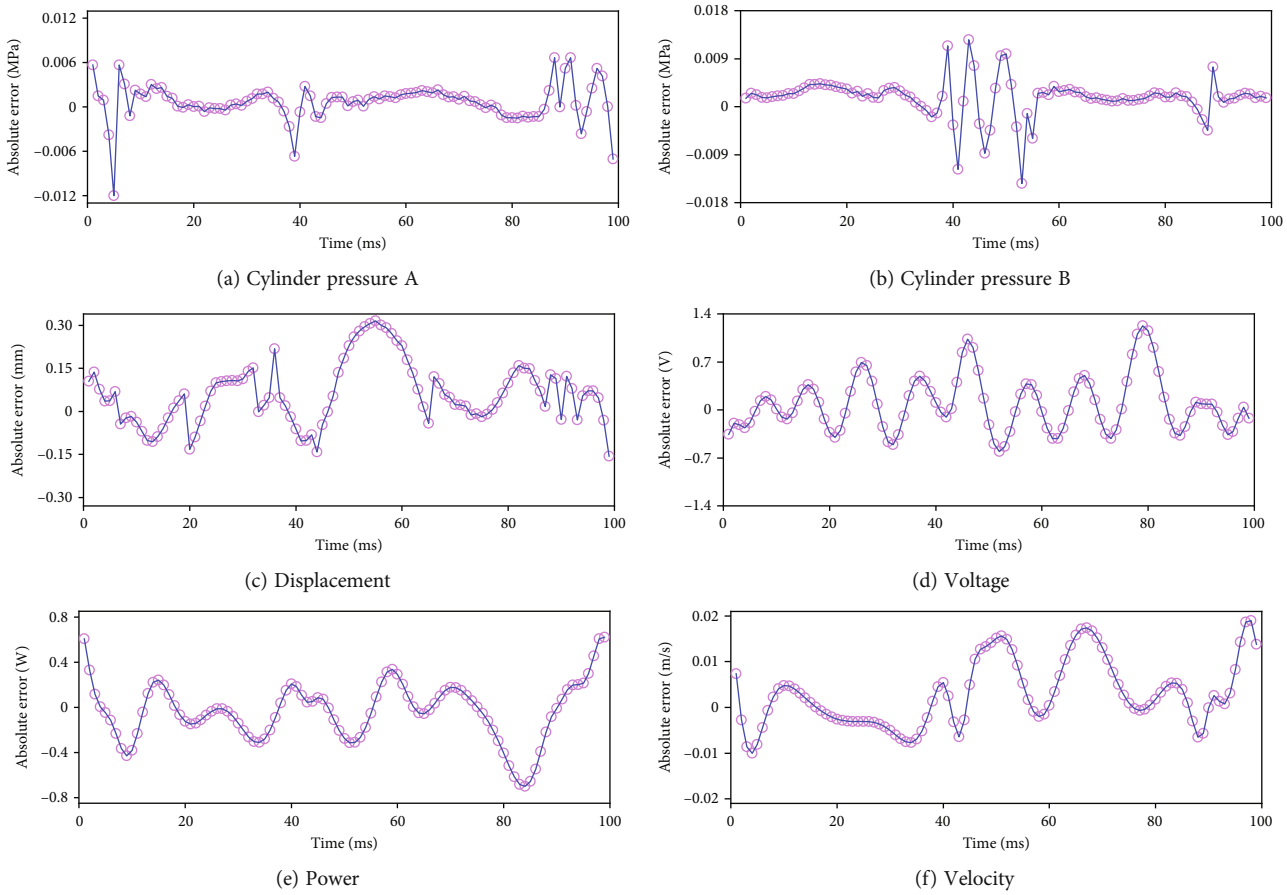


Figure 12: Absolute error of experimental and prediction results under the TCS.

accuracy as a whole, with significant deviations in prediction results only at certain points. The absolute errors of predicted cylinder pressures in chambers A and B are mostly less than 0.008 MPa, and it can be found that the places with larger errors appear near the peak cylinder pressure. The absolute error of PMA's displacement is below 0.5 mm, the absolute error of output voltage is between -0.7 V and 1 V, the absolute error of output power is basically within ±0.8 W, and the absolute error of PMA's velocity is between -0.01 m/s and 0.02 m/s. The error results indicate that the predictive ability of the BPNN model for the SFPE-LG under the TCS is considered acceptable.

Figure 13 shows the comparison of experimental and predicted results when the SFPE-LG operates under the PCS with an inlet pressure of 0.7 MPa, an intake duration of 20 ms, a load resistance of 100 Ω, and a preset stroke of 20-50 mm. Figure 14 gives the absolute errors between the prediction and experimental curves of the six output variables. The data shows that the predictive values of this BPNN model have good consistency with the experimental results under the PCS, with significant deviations only occurring at some inflection points. The absolute error of the cylinder pressures in working chambers A and B is mostly within ±0.007 MPa, the absolute error for the PMA's displacement is between -0.7 mm and 0.8 mm, the absolute error of the output voltage is within ±1.2 V, the absolute error of the output power is between -1 W and 0.5 W, and the absolute error for the PMA's velocity is mostly within ±0.016 m/s. These results indicate that the constructed BPNN model can be confidently adopted for predicting the output performance of SFPE-LG under PCS.

Table 7 lists the comparison between experimental and prediction results in terms of quantitative analysis (MSE, MAE, RMSE, and RMAE). These statistical values are all minimal, indicating that the developed BPNN model can better predict the output performance of the SFPE-LG. In conclusion, the established BPNN model can be applied to SFPE-LG running under TCS and PCS at the same time. However, there are differences in prediction accuracy for different output parameters.

*4.3. Hypothesis Testing (Wilcoxon Signed-Rank Test).* The Wilcoxon signed-rank test is used to perform hypothesis testing on the accuracy of the prediction results for the established BPNN model. The Wilcoxon signed-rank test, also known as the Wilcoxon signed-rank sum test and the Wilcoxon matched-paired test, is a nonparametric statistical test used to compare two dependent samples (namely, two groups consisting of matched or paired data points). Like other nonparametric tests, this test assumes that the data being analyzed does not require a specific distribution, e.g., whether or not it takes a normal distribution [54, 55].

The Wilcoxon signed-rank test requires two observation samples, such as the predicted results and actual results with

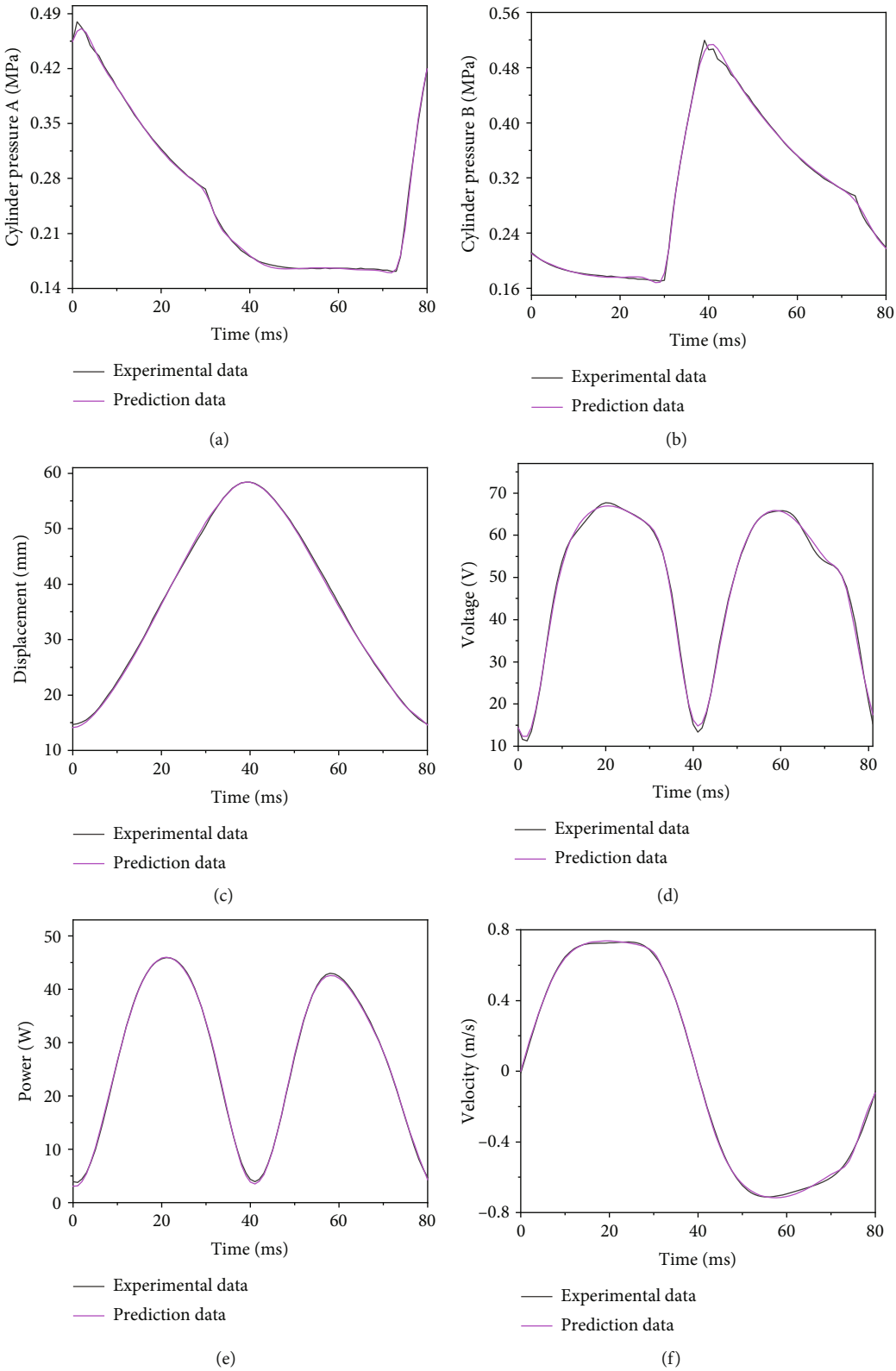


Figure 13: Comparison of experimental and prediction results under the PCS.

$N$ samples. In this study, the actual experimental results and predicted results are considered as two samples for the Wilcoxon signed-rank test. This test substantiates the proposed BPNN model to contribute mean difference between predicted and experimental results. The Wilcoxon signed-rank test is used to state the acceptance of null ($H_0$) and

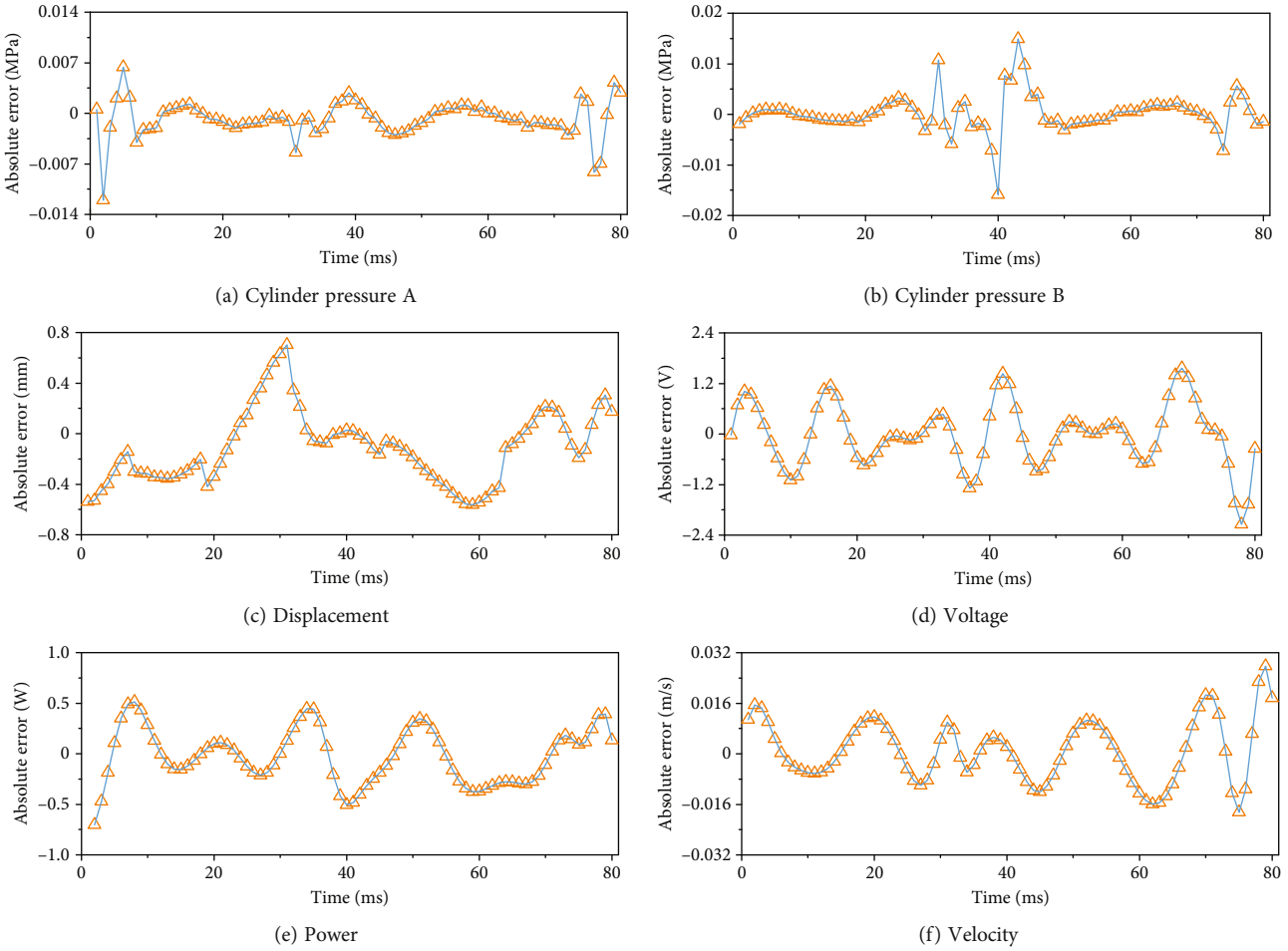


Figure 14: Absolute error of experimental and prediction results under the PCS.

Table 7: Comparative analysis of the BPNN model prediction results.

| Parameters | Strategy | MSE | MAE | RMSE | RMAE |
|---|---|---|---|---|---|
| Cylinder pressure A | TCS | 0.0000067 | 0.0017611 | 0.0025909 | 0.0419656 |
| | PCS | 0.0000072 | 0.0018398 | 0.0026849 | 0.0428924 |
| Cylinder pressure B | TCS | 0.0000163 | 0.0030739 | 0.0040333 | 0.0554431 |
| | PCS | 0.0000142 | 0.0023757 | 0.0037683 | 0.0487415 |
| Displacement | TCS | 0.0155932 | 0.0963890 | 0.1248725 | 0.3104658 |
| | PCS | 0.0989934 | 0.2567950 | 0.3146321 | 0.5067494 |
| Voltage | TCS | 0.1708170 | 0.3193996 | 0.4133002 | 0.5651545 |
| | PCS | 0.6159420 | 0.6022896 | 0.7848197 | 0.7760732 |
| Power | TCS | 0.0703732 | 0.2029715 | 0.2652795 | 0.4505236 |
| | PCS | 0.1110836 | 0.2566602 | 0.3332921 | 0.5066165 |
| Velocity | TCS | 0.0000614 | 0.0059993 | 0.0078326 | 0.0774551 |
| | PCS | 0.0001166 | 0.0085662 | 0.0107977 | 0.0925540 |

alternative ($H_1$) hypotheses. The null and alternative hypotheses adopted for this work are as follows.

$H_0$. The mean different is equal to zero.

$H_1$. The mean difference is not equal to zero.

The test statistic for the Wilcoxon signed-rank test is $W$, defined as $W+$ (sum of the positive ranks) and $W-$ (sum of the negative ranks). If the null hypothesis is true, we would expect to see similar numbers of lower and higher ranks that are both positive and negative (that is, $W+$ and $W-$ are similar). If a pair of scores are equal (the same value), then they are considered a tie and dropped from the analysis. Moreover, the critical considerations for

Table 8: The Wilcoxon signed-rank test results under the TCS.

| Parameters | Rank | $N$ | Mean rank | $Z$ statistic | $P$ value |
|---|---|---|---|---|---|
| Cylinder pressure A | $W-$ | 29 | 44.34 | -4.038 | ≤0.001 |
| | $W+$ | 69 | 51.667 | | |
| | Ties | 1 | | | |
| Cylinder pressure B | $W-$ | 15 | 59.97 | -5.499 | ≤0.001 |
| | $W+$ | 84 | 48.22 | | |
| | Ties | 0 | | | |
| Displacement | $W-$ | 31 | 34.84 | -4.869 | ≤0.001 |
| | $W+$ | 68 | 56.91 | | |
| | Ties | 0 | | | |
| Voltage | $W-$ | 48 | 43.88 | -1.288 | 0.198 |
| | $W+$ | 51 | 55.76 | | |
| | Ties | 0 | | | |
| Power | $W-$ | 54 | 52.31 | -1.222 | 0.222 |
| | $W+$ | 45 | 47.22 | | |
| | Ties | 0 | | | |
| Velocity | $W-$ | 40 | 39.83 | -3.078 | 0.002 |
| | $W+$ | 59 | 56.9 | | |
| | Ties | 0 | | | |

rejecting or accepting the null hypothesis depend on the $Z$ statistic value and the significance level of 5% ($\alpha = 0.05$). A $P$ value larger than the significance level fails to reject the null hypothesis, whereas a $P$ value smaller than the significance level rejects the null hypothesis.

Table 8 shows the Wilcoxon signed-rank test results when the BPNN model is used to predict the output performance of SFPE-LG under the TCS. The $P$ values for cylinder pressures A and B, displacement, and velocity are less than 0.05, which indicates that there is evidence to reject the null hypothesis with a significance level of 95%. The $P$ values for the output voltage and power are greater than 0.05, which indicates acceptance of the null hypothesis. Therefore, the cylinder pressures in chambers A and B, displacement, and velocity of the PMA predicted by the established BPNN model are significantly different from the experimental results under the TCS, while the predicted output voltage and power results are not significantly different from the experimental results.

Table 9 tabulates the Wilcoxon signed-rank test results when the BPNN model is used to predict the output results of SFPE-LG under the PCS. The $P$ values for cylinder pressures A and displacement are less than 0.05, which indicates the evidence to reject the null hypothesis at a significance level of 95%. The $P$ values of the cylinder pressures B, velocity, output voltage, and power are greater than 0.05, which suggests acceptance of the null hypothesis. Therefore, the cylinder pressures in chamber A and displacement of the PMA predicted by the BPNN model are significantly different from the experimental results under the PCS. The other predicted results are not significantly different from the experimental results. This also reveals that the prediction accuracy of the BPNN model for the output performance of SFPE-LG running under the PCS is significantly better than the output results running under the TCS. The positive ($W+$) and negative ($W-$) ranks of cylinder pressure B, voltage, and velocity are approximately equal, which shows that the established BPNN model has higher prediction accuracy for cylinder pressure in chamber B, output voltage, and velocity of the PMA under the PCS.

Table 9: The Wilcoxon signed-rank test under the PCS.

| Parameters | Rank ($R$) | $N$ | Mean rank | $Z$ statistic | $P$ value |
|---|---|---|---|---|---|
| Cylinder pressure A | $W-$ | 53 | 44.92 | -3.141 | 0.002 |
| | $W+$ | 29 | 35.24 | | |
| | Ties | 0 | — | | |
| Cylinder pressure B | $W-$ | 42 | 40.75 | -0.046 | 0.963 |
| | $W+$ | 40 | 42.29 | | |
| | Ties | 0 | — | | |
| Displacement | $W-$ | 57 | 43.86 | -3.691 | ≤0.001 |
| | $W+$ | 25 | 36.12 | | |
| | Ties | 0 | — | | |
| Voltage | $W-$ | 41 | 40.71 | -0.150 | 0.881 |
| | $W+$ | 41 | 42.29 | | |
| | Ties | 0 | — | | |
| Power | $W-$ | 46 | 42.91 | -1.260 | 0.208 |
| | $W+$ | 36 | 42.29 | | |
| | Ties | 0 | — | | |
| Velocity | $W-$ | 40 | 40.31 | -0.411 | 0.681 |
| | $W+$ | 42 | 42.63 | | |
| | Ties | 0 | — | | |

Table 10: Optimization variable value range for the BPNN model.

| Optimization variable | Minimum | Maximum | Units |
|---|---|---|---|
| Inlet pressure ($p_{in}$) | 0.2 | 0.7 | MPa |
| Intake duration ($t_{in}$) | 15 | 35 | ms |
| Expansion duration ($t_{ex}$) | 70 | 120 | ms |
| Load resistance ($R$) | 20 | 110 | $\Omega$ |
| Preset stroke ($S_p$) | 15-55 | 10-60 | mm |

*4.4. Optimization of Output Power.* The motion characteristics and output performance for the SFPE-LG are affected by multiple factors under different working conditions based on experimental data [47, 48]. The output power is a critical evaluation index considered in engineering applications. To get optimal system performance and working parameters, the maximum output power of SFPE-LG was optimized by using this established BPNN model coupled with GA. The output power prediction model of the SFPE-LG can be

Table 11: Optimization results from the BPNN and GA models.

| Operation strategy | Optimization variable | Values | Units |
|---|---|---|---|
| Time control strategy | Inlet pressure ($p_{in}$) | 0.7 | MPa |
| | Intake duration ($t_{in}$) | 35 | ms |
| | Expansion duration ($t_{ex}$) | 104 | ms |
| | Load resistance ($R$) | 67 | $\Omega$ |
| | Output power ($P_{out}$) | 141.69 | W |
| Position control strategy | Inlet pressure ($p_{in}$) | 0.65 | MPa |
| | Intake duration ($t_{in}$) | 35 | ms |
| | Load resistance ($R$) | 102 | $\Omega$ |
| | Preset stroke ($S_p$) | 11-59 | mm |
| | Output power ($P_{out}$) | 138.03 | W |

regarded as a multivariate function. The search and optimization process of GA can be seen as the process of finding the optimum solution for multivariate functions. The optimization process is shown in Figure 5, and the optimization function can be expressed as equations (3) and (4). Under the two control strategies, five operating parameters including inlet pressure, load resistance, intake duration, expansion duration, and preset stroke were selected as optimization variables. The value range for each optimization variable is shown in Table 10.

$$\mathrm{TCS}: \mathrm{Max}\,(P_{out}) = f(p_{in}, t_{in}, t_{ex}, R), \tag{3}$$

$$\mathrm{PCS}: \mathrm{Max}\,(P_{out}) = f\left(p_{in}, t_{in}, R, S_p\right). \tag{4}$$

Table 11 provides the optimization results of this SFPE-LG based on constructed BPNN and GA models. These data indicate that the maximum output power of this SFPE-LG can achieve 141.69 W under the TCS, and the corresponding operating parameters of inlet pressure, intake duration, expansion duration, and load resistance are 0.7 MPa, 35 ms, 67 $\Omega$, and 104 ms, respectively. When the SFPE-LG works on the PCS, it can achieve a maximum output power of 138.03 W, with corresponding operating parameters of $p_{in} = 0.65$ MPa, $t_{in} = 35$ ms, $R = 102\,\Omega$, and $S_p = 11 - 59$ mm. The differences in maximum output power between the time and position control strategies are small, which means that the multiple-point operating conditions can achieve the same output power target.

## 5. Conclusions

This paper established a test bench for the SFPE-LG system and proposed two kinds of valve timing control strategies, namely, TCS and PCS. Based on the experimental data, a BPNN performance prediction model of the SFPE-LG prototype was established and validated. Then, the influences of parameters such as the number of neural network layers, transfer function, training function, number of HLNs, and LR on the predictive accuracy for this BPNN model were discussed, and the optimal parameter settings were determined. Moreover, the 5-fold cross-validation and Wilcoxon signed-rank test are adopted to verify the training and prediction accuracy of the BPNN model. Finally, the predictive model was integrated with the GA to predict and optimize the output power of SFPE-LG at full working conditions. The main findings are summarized below:

(1) The BPNN model developed for predicting the motion characteristics and output performance of the SFPE-LG exhibits strong learning and prediction abilities under the two control strategies. The prediction accuracy of the BPNN model for the output performance of the SFPE-LG running under the PCS is significantly better than that of operating under the TCS

(2) Different neural network layers, transfer functions, training functions, hidden layer nodes, and learning rates directly influence the prediction accuracy of the BPNN model. HLN has a greater impact on MSE and correlation coefficient than that of the learning rate. When the number of HLNs is more than 30, the BPNN model has low MSE and high correlation coefficient regardless of the learning rate value

(3) The optimization results of the BPNN model combined with GA show that the maximum output power of the SFPE-LG can achieve 141.69 W under the TCS, and the corresponding working parameters are as follows: $p_{in} = 0.7$ MPa, $t_{in} = 35$ ms, $R = 67\,\Omega$, and $t_{ex} = 104$ ms. The maximum output power of the SFPE-LG can reach 138.03 W under the PCS with corresponding operating parameters of $p_{in} = 0.65$ MPa, $t_{in} = 35$ ms, $R = 102\,\Omega$, and $S_p = 11 - 59$ mm

(4) The simulation results of the SFPE-LG output performance prediction and optimization model based on machine learning and genetic algorithm can give valuable guidance for experiments, so as to quickly and accurately obtain the maximum output power and corresponding working parameters

This paper mainly predicts and optimizes the motion characteristics and output power of the SFPE-LG and lacks

the study of the energy conversion efficiency. Therefore, the next step should be to conduct a detailed analysis of the thermal-work, work-electric, and thermal-electric conversion efficiencies for the SFPE-LG based on the optimization results in this paper. Then, a combination of machine learning and optimization algorithms is used to perform multiobjective optimization on the indexes of output power and energy conversion efficiency. The analysis results will provide important guidance for improving the output power and overall energy conversion efficiency of the SFPE-LG, so that the SFPE-LG can obtain maximum output power while maintaining high energy conversion efficiency.

## Nomenclature

*Symbols*

$f$: Operating frequency (Hz)
$P_{out}$: Output power (W)
$p_{in}$: Inlet pressure (MPa)
$P_1$, $P_2$: Preset displacement point (mm)
$R$: Load resistance ($\Omega$)
$S_a$: Actual stroke (mm)
$S_p$: Preset stroke (mm)
$S_m$: Maximum stroke (mm)
$t_{in}$: Intake duration (mm)
$t_{ex}$: Expansion duration (ms)
$H_0$: Null hypothesis (-)
$H_1$: Alternative hypothesis (-).

*Abbreviations*

ANN: Artificial neural network
BDC: Bottom dead center
BPNN: Back propagation neural network
FPEG: Free piston expander
GA: Genetic algorithm
HLN: Hidden layer nodes
ICE: Internal combustion engine
LR: Learning rate
MAE: Mean absolute error
MAPE: Mean absolute percentage error
MSE: Mean square error
ORC: Organic Rankine cycle
PCS: Position control strategy
PMA: Piston mover assembly
PMLG: Permanent magnet linear generator
$R$: Correlation coefficient
RMAE: Root mean absolute error
RMSE: Root mean square error
SFPE-LG: Single-piston free piston expander-linear generator
TCS: Time control strategy
TDC: Top dead center.

## Data Availability

Data are available on request.

## Conflicts of Interest

The authors declare that they have no conflicts of interest.

## Acknowledgments

This work is supported by the National Natural Science Foundation of China (Grant No. 52005038) and the Beijing Natural Science Foundation (Grant No. 3222024).

## References

[1] F. Yang, H. Zhang, C. Bei, S. Song, and E. Wang, "Parametric optimization and performance analysis of ORC (organic Rankine cycle) for diesel engine waste heat recovery with a fin-and-tube evaporator," *Energy*, vol. 91, pp. 128–141, 2015.

[2] S. Bai and C. Liu, "Overview of energy harvesting and emission reduction technologies in hybrid electric vehicles," *Renewable and Sustainable Energy Reviews*, vol. 147, article 111188, 2021.

[3] F. Yang, X. Dong, H. Zhang et al., "Performance analysis of waste heat recovery with a dual loop organic Rankine cycle (ORC) system for diesel engine under various operating conditions," *Energy Conversion and Management*, vol. 80, pp. 243–255, 2014.

[4] E. Wang, Z. Yu, H. Zhang, and F. Yang, "A regenerative supercritical-subcritical dual-loop organic Rankine cycle system for energy recovery from the waste heat of internal combustion engines," *Applied Energy*, vol. 190, pp. 574–590, 2017.

[5] Y. Xu, H. Zhang, F. Yang et al., "Experimental study on small power generation energy storage device based on pneumatic motor and compressed air," *Energy Conversion and Management*, vol. 234, article 113949, 2021.

[6] B. Xu, D. Rathod, A. Yebi, Z. Filipi, S. Onori, and M. Hoffman, "A comprehensive review of organic Rankine cycle waste heat recovery systems in heavy-duty diesel engine applications," *Renewable and Sustainable Energy Reviews*, vol. 107, pp. 145–170, 2019.

[7] L. Shi, G. Shu, H. Tian, and S. Deng, "A review of modified organic Rankine cycles (ORCs) for internal combustion engine waste heat recovery (ICE-WHR)," *Renewable and Sustainable Energy Reviews*, vol. 92, pp. 95–110, 2018.

[8] J. Sachdeva and O. Singh, "Thermodynamic analysis of solar powered triple combined Brayton, Rankine and organic Rankine cycle for carbon free power," *Renewable Energy*, vol. 139, pp. 765–780, 2019.

[9] K. Rahbar, S. Mahmoud, R. K. Al-Dadah, and N. Moazami, "Review of organic Rankine cycle for small-scale applications," *Energy Conversion and Management*, vol. 134, pp. 135–155, 2017.

[10] H. Tian, G. Shu, H. Wei, X. Liang, and L. Liu, "Fluids and parameters optimization for the organic Rankine cycles (ORCs) used in exhaust heat recovery of internal combustion engine (ICE)," *Energy*, vol. 47, no. 1, pp. 125–136, 2012.

[11] C. Sprouse III and C. Depcik, "Review of organic Rankine cycles for internal combustion engine exhaust waste heat recovery," *Applied Thermal Engineering*, vol. 51, no. 1-2, pp. 711–722, 2013.

[12] J. Zhang, H. Zhang, K. Yang et al., "Performance analysis of regenerative organic Rankine cycle (RORC) using the pure working fluid and the zeotropic mixture over the whole operating range of a diesel engine," *Energy Conversion and Management*, vol. 84, pp. 282–294, 2014.

[13] F. Pantano and R. Capata, "Expander selection for an on board ORC energy recovery system," *Energy*, vol. 141, pp. 1084–1096, 2017.

[14] P. Song, M. Wei, L. Shi, S. N. Danish, and C. Ma, "A review of scroll expanders for organic Rankine cycle systems," *Applied Thermal Engineering*, vol. 75, pp. 54–64, 2015.

[15] A. Costall, A. Hernandez, P. J. Newton, and R. F. Martinez-Botas, "Design methodology for radial turbo expanders in mobile organic Rankine cycle applications," *Applied Energy*, vol. 157, pp. 729–743, 2015.

[16] O. Dumont, A. Parthoens, R. Dickes, and V. Lemort, "Experimental investigation and optimal performance assessment of four volumetric expanders (scroll, screw, piston and roots) tested in a small-scale organic Rankine cycle system," *Energy*, vol. 165, pp. 1119–1127, 2018.

[17] S. Emhardt, G. Tian, and J. Chew, "A review of scroll expander geometries and their performance," *Applied Thermal Engineering*, vol. 141, pp. 1020–1034, 2018.

[18] X. Hou, H. Zhang, Y. Xu et al., "External load resistance effect on the free piston expander-linear generator for organic Rankine cycle waste heat recovery system," *Applied Energy*, vol. 212, pp. 1252–1261, 2018.

[19] J. Bao and L. Zhao, "A review of working fluid and expander selections for organic Rankine cycle," *Renewable and Sustainable Energy Reviews*, vol. 24, pp. 325–342, 2013.

[20] R. Mikalsen and A. P. Roskilly, "A review of free-piston engine history and applications," *Applied Thermal Engineering*, vol. 27, no. 14-15, pp. 2339–2352, 2007.

[21] J. Li, Z. Zuo, B. Jia et al., "Comparative analysis on friction characteristics between free-piston engine generator and traditional crankshaft engine," *Energy Conversion and Management*, vol. 245, article 114630, 2021.

[22] Y. Xu, L. Tong, H. Zhang et al., "Experimental and simulation study of a free piston expander-linear generator for small-scale organic Rankine cycle," *Energy*, vol. 161, pp. 776–791, 2018.

[23] H. Feng, Z. Zhang, B. Jia, Z. Zuo, A. Smallbone, and A. P. Roskilly, "Investigation of the optimum operating condition of a dual piston type free piston engine generator during engine cold start-up process," *Applied Thermal Engineering*, vol. 182, article 116124, 2021.

[24] F. Yang, H. Zhang, X. Hou, Y. Tian, and Y. Xu, "Experimental study and artificial neural network based prediction of a free piston expander-linear generator for small scale organic Rankine cycle," *Energy*, vol. 175, pp. 630–644, 2019.

[25] P. Heyl and H. Quack, "Free piston expander-compressor for $CO_2$-design, applications and results," in *Proceedings of the 20th international congress of refrigeration Sydney*, Sydney, 1999.

[26] S. Burugupally and L. Weiss, "Power generation via small length scale thermo-mechanical systems: current status and challenges, a review," *Energies*, vol. 11, no. 9, p. 2253, 2018.

[27] S. Burugupally and L. Weiss, "Design and performance of a miniature free piston expander," *Energy*, vol. 170, pp. 611–618, 2019.

[28] L. Weiss, "Study of a MEMS-based free piston expander for energy sustainability," *Journal of Mechanical Design*, vol. 132, no. 9, pp. 91002–91008, 2010.

[29] C. Champagne and L. Weiss, "Performance analysis of a miniature free piston expander for waste heat energy harvesting," *Energy Conversion and Management*, vol. 76, pp. 883–892, 2013.

[30] B. Preetham and L. Weiss, "Investigations of a new free piston expander engine cycle," *Energy*, vol. 106, pp. 535–545, 2016.

[31] F. Kodakoglu, *Performance Analysis on Free-Piston Linear Expander*, University of North Florida, America, 2017.

[32] A. R. A. Aziz, M. A. Ismael, E. Z. Zainal, S. E. Mohammed, M. B. Baharom, and A. R. T. Anwarudin, "Effect of generator configuration on the free-piston motion and power generation of air-driven expander system," *Alexandria Engineering Journal*, vol. 61, no. 4, pp. 3093–3104, 2022.

[33] M. A. Ismael, A. R. A. Aziz, Z. Zainal et al., "Investigation on free-piston motion and power generation of a dual-piston air-driven expander linear generator," *Energy Reports*, vol. 7, pp. 2388–2397, 2021.

[34] Y. Wang, L. Chen, B. Jia, and A. P. Roskilly, "Experimental study of the operation characteristics of an air-driven free-piston linear expander," *Applied Energy*, vol. 195, pp. 93–99, 2017.

[35] X. Hou, Y. Liu, X. Qi et al., "Performance analysis of free piston linear generator coupling organic Rankine cycle system for waste heat recovery," *Applied Thermal Engineering*, vol. 193, article 116991, 2021.

[36] X. Hou, H. Zhang, T. Zhao et al., "Study on the control strategy of free piston expander-linear generator used for organic Rankine cycle waste heat recovery," *Journal of Thermal Science*, vol. 30, no. 2, pp. 585–597, 2021.

[37] Y. Tian, H. Zhang, J. Li et al., "Development and validation of a single-piston free piston expander-linear generator for a small-scale organic Rankine cycle," *Energy*, vol. 161, pp. 809–820, 2018.

[38] Z. Wu, H. Zhang, Z. Liu et al., "Experimental study on the performance of single-piston free-piston expander-linear generator," *Energy*, vol. 221, article 119724, 2021.

[39] Y. Feng, K. Xu, Q. Zhang et al., "Experimental investigation and machine learning optimization of a small-scale organic Rankine cycle," *Applied Thermal Engineering*, vol. 224, article 120120, 2023.

[40] K. Sudheer, A. Gosain, and K. Ramasastri, "A data-driven algorithm for constructing artificial neural network rainfall-runoff models," *Hydrological Processes*, vol. 16, no. 6, pp. 1325–1330, 2002.

[41] S. Das, T. P. Sahu, R. R. Janghel, and B. K. Sahu, "Effective forecasting of stock market price by using extreme learning machine optimized by PSO-based group oriented crow search algorithm," *Neural Computing and Applications*, vol. 34, no. 1, pp. 555–591, 2022.

[42] F. Yang, H. Cho, H. Zhang, J. Zhang, and Y. Wu, "Artificial neural network (ANN) based prediction and optimization of an organic Rankine cycle (ORC) for diesel engine waste heat recovery," *Energy Conversion and Management*, vol. 164, pp. 15–26, 2018.

[43] J. S. Kim, D. Y. Kim, and Y. T. Kim, "Experiment on radial inflow turbines and performance prediction using deep neural network for the organic Rankine cycle," *Applied Thermal Engineering*, vol. 149, pp. 633–643, 2019.

[44] L. Palagi, E. Sciubba, and L. Tocci, "A neural network approach to the combined multi-objective optimization of the thermodynamic cycle and the radial inflow turbine for organic Rankine cycle applications," *Applied Energy*, vol. 237, pp. 210–226, 2019.

[45] Z. Tian, W. Gan, X. Zou, Y. Zhang, and W. Gao, "Performance prediction of a cryogenic organic Rankine cycle based on back

propagation neural network optimized by genetic algorithm," *Energy*, vol. 254, article 124027, 2022.

[46] J. Subramanian, *Design, Modeling and Optimization of Reciprocating Tubular Permanent Magnet Linear Generators for Free Piston Engine Applications*, West Virginia University, 2020.

[47] J. Li, F. Yang, H. Zhang et al., "Comparative analysis of different valve timing control methods for single-piston free piston expander-linear generator via an orthogonal experimental design," *Energy*, vol. 195, article 116966, 2020.

[48] J. Li, H. Zhang, Y. Tian et al., "Performance analysis of a single-piston free piston expander-linear generator with intake timing control strategy based on piston displacement," *Applied Thermal Engineering*, vol. 152, pp. 751–761, 2019.

[49] K. Hamdia, X. Zhuang, and T. Rabczuk, "An efficient optimization approach for designing machine learning models based on genetic algorithm," *Neural Computing and Applications*, vol. 33, no. 6, pp. 1923–1933, 2021.

[50] N. A. Nariman, K. Hamdia, A. M. Ramadan, and H. Sadaghian, "Optimum design of flexural strength and stiffness for reinforced concrete beams using machine learning," *Applied Sciences*, vol. 11, no. 18, p. 8762, 2021.

[51] D. Sami Khafaga, A. Ali Alhussan, E. M. El-kenawy et al., "Improved prediction of metamaterial antenna bandwidth using adaptive optimization of LSTM," *Computers, Materials & Continua*, vol. 73, no. 1, pp. 865–881, 2022.

[52] E. M. El-Kenawy, B. Zerouali, N. Bailek et al., "Improved weighted ensemble learning for predicting the daily reference evapotranspiration under the semi-arid climate conditions," *Environmental Science and Pollution Research*, vol. 29, no. 54, pp. 81279–81299, 2022.

[53] M. Dorofki, A. H. Elshafie, O. Jaafar, O. A. Karim, and S. Mastura, "Comparison of artificial neural network transfer functions abilities to simulate extreme runoff data," *International Proceedings of Chemical, Biological and Environmental Engineering*, vol. 33, pp. 39–44, 2012.

[54] S. Das, T. P. Sahu, and R. R. Janghel, "Stock market forecasting using intrinsic time-scale decomposition in fusion with cluster based modified CSA optimized ELM," *Journal of King Saud University-Computer and Information Sciences*, vol. 34, no. 10, pp. 8777–8793, 2022.

[55] S. Das, T. P. Sahu, and R. R. Janghel, "Oil and gold price prediction using optimized fuzzy inference system based extreme learning machine," *Resources Policy*, vol. 79, article 103109, 2022.